Sfrp2 is a multifunctional regulator of rodent color patterns

Matthew R. Johnson[1*], Sha Li[1*], Christian F. Guerrero-Juarez[2,3,4,5,6], Pearson Miller[7], Benjamin J. Brack[1], Sarah A. Mereby[1], Charles Feigin[1], Jenna Gaska[1], Qing Nie[3,4,5,6], Jaime A. Rivera-Perez[8], Alexander Ploss[1], Stanislav Y. Shvartsman[1,7], and Ricardo Mallarino[1+]

[1]Department of Molecular Biology, Princeton University; Princeton, New Jersey, 08540, USA.

[2]Carle Illinois College of Medicine, University of Illinois at Urbana-Champaign, Urbana, IL 61801 USA.

[3]Department of Developmental and Cell Biology, University of California, Irvine, Irvine, CA 92697, USA.

[4]Department of Mathematics, University of California, Irvine, Irvine, CA, 92697, USA

[5]Center for Complex Biological Systems, University of California, Irvine, Irvine, CA 92697, USA

[6]NSF-Simons Center for Multiscale Cell Fate Research, University of California, Irvine, Irvine, CA, 92697, USA

[7]Center for Computational Biology, Developmental Dynamics, Flatiron Institute, Simons Foundation; New York, New York, 10010, USA.

[8]University of Massachusetts Chan Medical School, Worcester, MA 01655, USA

*Equal contributions

[+]Corresponding author. Email: rmallarino@princeton.edu

Summary

Animal color patterns are strikingly diverse and can serve as a useful model for understanding how tissues acquire positional information. Here, we study the coat of the African striped mouse (*Rhabdomys pumilio*) to uncover mechanisms regulating the formation of stripe patterns. By combining transcriptomic profiling, mathematical modeling, mouse transgenics, and *in vivo* gene editing in striped mice, we show that the Wnt modulator, *Sfrp2*, plays two distinct roles in stripe patterning. During embryogenesis, it regulates patterns of hair placode formation, producing the embryonic prepattern that foreshadows pigment stripes while, in postnatal stages, it modulates differences in hair color. This dual effect is achieved through spatiotemporal shifts in expression and opposing effects on Wnt signaling within the same tissue. Thus, by uncovering a multifunctional regulator of stripe formation, our work provides insights into the mechanisms by which spatial patterns are established in developing embryos and the molecular basis of phenotypic novelty.

Introduction

During embryogenesis, skin develops via reciprocal interactions between the epithelial cells that give rise to the epidermis and the underlying mesodermal cells that originate the dermis (Fuchs, 2007). This core developmental program is locally modified within a single organism, leading to marked spatial differences in thickness, pigmentation, and types of cutaneous appendages (Fuchs and Raghavan, 2002; Johansson and Headon, 2014). Such extraordinary variation evidences the rich complexity of the skin's underlying gene regulatory code and makes this tissue a fascinating model for understanding both the mechanisms that generate spatially restricted morphological patterns and the molecular basis of phenotypic diversity.

The skin of many vertebrate species displays characteristic periodic pigment patterns, such as spots and stripes, which play key roles in mediating intra- and inter-specific communication (Caro, 2005; Caro and Mallarino, 2020; Mills and Patterson, 2009). Theoretical simulations involving Turing reaction-diffusion systems, in which activators and inhibitors interact to establish organized spatial patterns, can closely recapitulate a wide variety of periodic color patterns seen in nature (Kondo, 2017; Kondo and Miura, 2010; Turing, 1990). Notably, however, Turing-generated patterns are variable and sensitive to stochastic perturbations (Vittadello et al., 2021). That is, Turing mechanisms are insufficient, by themselves, to explain the formation of periodic color patterns seen in many species, which are characterized by a high degree of spatial organization and reproducibility across individuals (Haupaix and Manceau, 2020; Kaelin et al., 2012, 2021; Mallarino et al., 2016; Patterson and Parichy, 2019). Therefore, a long-standing challenge has been to uncover the molecular, cellular, and developmental events by which periodic color patterns are specified and organized.

The African striped mouse (*Rhabdomys pumilio*), a rodent that exhibits a naturally evolved coat pattern of dark and light parallel stripes (Fig. 1A, B), is a useful model in which to explore molecular mechanisms underlying periodic color patterns because this mouse can be maintained and reared in the lab, allowing for controlled experiments and development of molecular tools (Mallarino et al., 2018). Here, we use a variety of multidisciplinary approaches to uncover the developmental mechanisms controlling coat pattern formation in striped mice.

Results

Striped mice display regional variation in embryonic placode formation

Striped mice exhibit differences in hair length between striped skin regions that are apparent at early postnatal stages (Fig. 1B) (Mallarino et al., 2016). We hypothesized that these differences may reflect stripe-specific alterations in the developmental timing of hair follicle placodes (hereafter referred to as placodes). In laboratory mice (*Mus musculus*), placodes are visible at embryonic day 15.5 (E15.5) and are evenly distributed throughout the dorsal skin (Fig. 1C) (Hardy, 1992; Millar, 2002). Remarkably, this stereotyped spatial pattern differs considerably in striped mice. At the equivalent embryonic stage (*i.e.*, the emergence of visible placodes, ~E16.5 in striped mice), whole mount *in situ* hybridizations for early markers of placode formation (e.g., *Dkk4*, *Ctnnb1*, *Wnt10b*, *Wif1*, *Eda*, and *Dkk1*) (Andl et al., 2002) revealed that striped mouse dorsal placodes develop in a stripe-like, spatially restricted manner, whereby they are present in some regions along the dorsal skin but absent in others (Fig. 1C and Fig. S1). Approximately two days later, at E18.5, placodes eventually become visible in regions previously devoid of them, as evidenced by thickening of the epidermis and the appearance of molecular markers (Fig. S2). Notably, stripe-like dorsal areas where placodes fail to form initially correspond to regions that

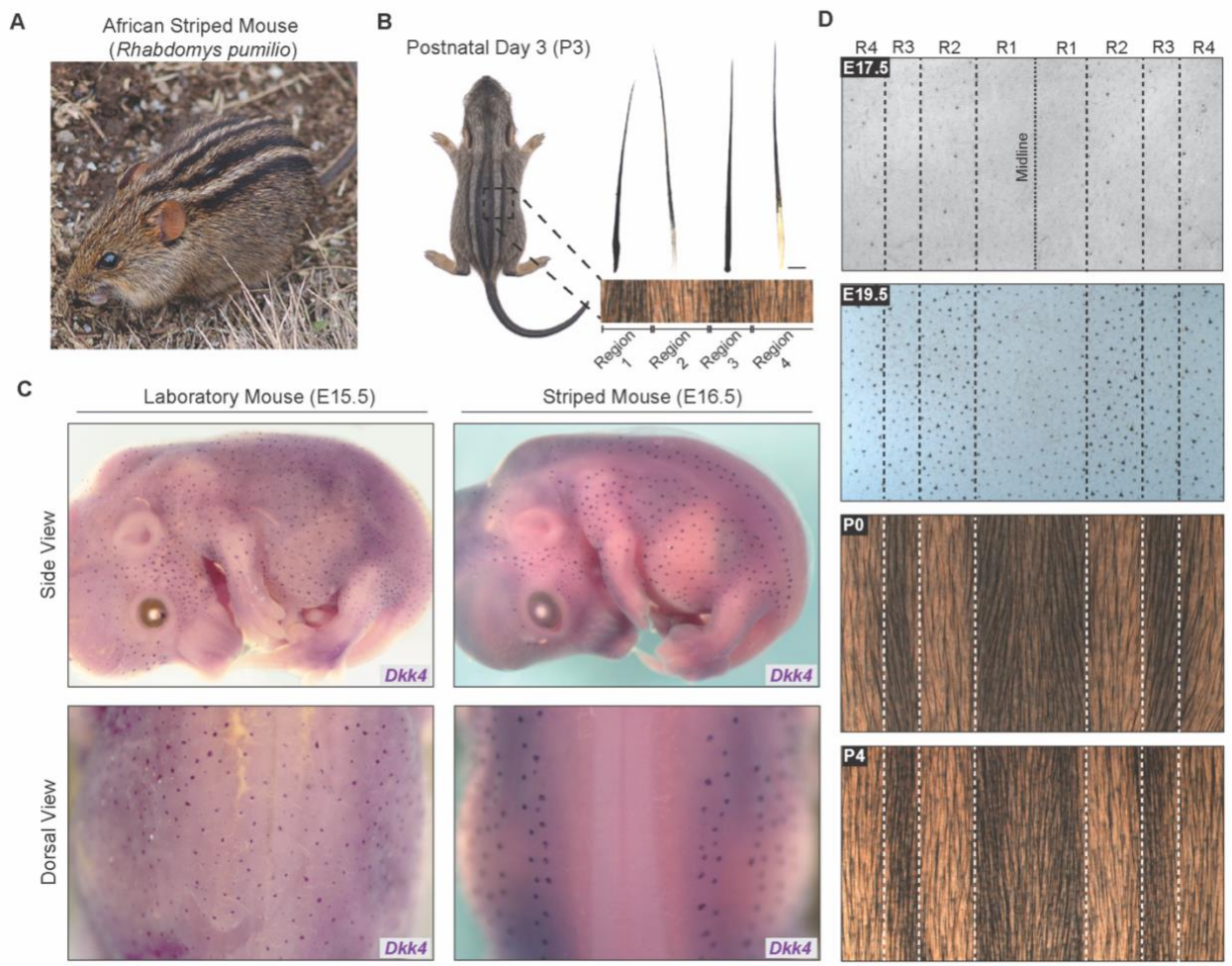

Figure 1. Development of hair placodes and pigment patterns in the African striped mouse. (A) An adult striped mouse in the field. (B) Postnatal Day 3 (P3) striped mouse pup displaying the characteristic striped pattern and corresponding differences in hair length across dorsal regions. (C) Side and dorsal views of Embryonic Day 15.5 (E15.5) laboratory mouse and E16.5 striped mouse embryos displaying spatial patterns of hair placode formation, as visualized by whole-mount *in situ* hybridization for *Dkk4*. (D) Light-microscopy images of striped mouse flat-mount skins from developmental and postnatal stages (E16.5 to P4) showing how patterns of hair placode development foreshadow pigmentation stripes. Photo credit in (A): Trevor Hardaker

will constitute the eventual dark pigment stripes, explaining why hair from dark stripes is shorter at birth and suggesting that spatially restricted patterns of embryonic placode formation foreshadow pigmentation stripes (Fig. 1D) (Mallarino et al., 2016).

Transcriptomic profiling and mathematical modeling identify a potential regulator of placode formation

To identify regulators of the striped mouse placode developmental pattern, we performed an unbiased bulk-level RNA-sequencing (RNA-seq) screen for genes differentially expressed between placode rich and placode barren skin regions in E16.5 embryos. We used the boundaries between these regions as a proxy to mark and isolate four distinct dorsal skin regions: R1 (the dorsalmost, placode barren region), R2 (the dorsalmost, placode rich region), R3 (the ventralmost, placode barren region), and R4 (the ventralmost, placode rich region) (Fig. 2A). After data processing and read mapping (see STAR Methods), we performed a series of pairwise comparisons (R1 vs. R2; R1 vs. R4; R2 vs. R3; and R3 vs. R4) to identify differentially expressed genes between placode barren (R1, R3) and placode rich (R2, R4) regions. Although each pairwise comparison yielded several differentially expressed genes (Fig. 2B, Table S1), only one gene, *Sfrp2*, was differentially expressed in all four comparisons. Surprisingly, however, *Sfrp2* was neither up nor downregulated in placode barren (R1, R3) or placode rich regions (R2, R4). Rather, this gene was always upregulated in the dorsalmost region among the two being compared (*i.e.*, R1>R2, R1>R4, R2>R3, and R3>R4). Indeed, when we extended our comparisons to include R1 vs. R3 and R2 vs. R4, we confirmed that *Sfrp2* was differentially expressed among these regions in a dorsoventral gradient (i.e., R1>R3 and R2>R4) (Fig. S3).

The dorsoventral expression pattern of a potential regulator of placode patterning was, *a priori*, unexpected. However, previous theoretical work has pointed to upstream morphogen gradients as a means for establishing stripe-like patterns (Hiscock and Megason, 2015). In mammals, placode spacing is regulated by a self-organizing Turing reaction-diffusion system in which

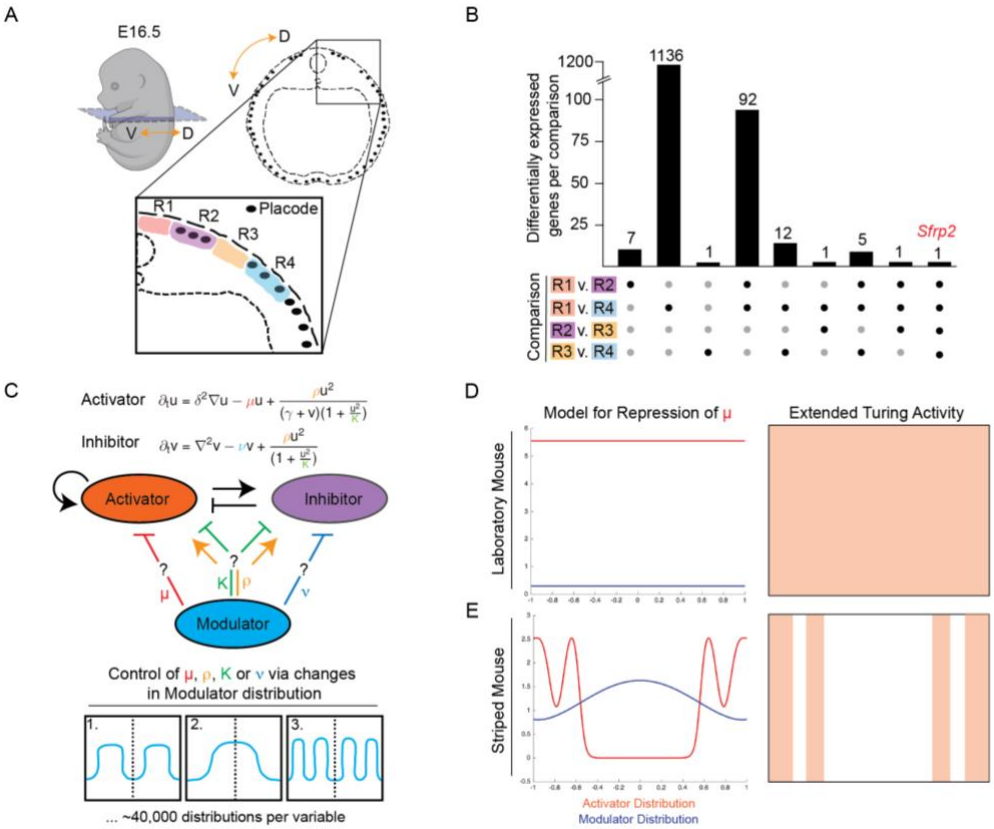

Figure 2. Transcriptomics and mathematical modeling of placode development. (A) Schematic of a striped mouse E16.5 embryo and cross section displaying the regions (R1, R2, R3, R4) that were dissected for bulk-level RNA-seq analysis. Placodes are visible in R2 and R4 but not in R1 and R3. (B) UpSet plot summarizing genes differentially expressed (padj < 0.05) between Regions 1-4. Each row of dots represents a single pairwise comparison. Black dots indicate there were differentially expressed genes between a given comparison (number of differentially expressed genes plotted as columns) whereas grey dots indicate there were not. (C-E) Mathematical simulations of hair placode spacing in laboratory mouse and in striped mouse. (C) Equations used to model how a theoretical modulator (blue) could guide the activity of an activator-inhibitor reaction-diffusion system. Four parameters ($\mu, \nu, \rho,$ and K) governing chemical kinetics and representative of distinct mechanisms through which a modulator could influence patterning were tested. Approximately ~40,000 modulator distributions were tested for each parameter. (D) Simulations of a uniform modulator expression pattern (blue line) on variable μ produces a uniform pattern of Turing activity. This pattern is consistent with what is seen in laboratory mice *in vivo* (Fig. 1C). (E) Simulations in which a dorsoventral gradient of a modulator (blue line) applied to the same system in (D), leads to a stripe-like pattern of Turing activity. This recapitulates what is seen in striped mice *in vivo* (Fig 1C).

activators and inhibitors interact to establish an organized spatial pattern (Sick et al., 2006). We therefore used mathematical modeling to ask whether a dorsoventral gradient could guide the establishment of parallel stripes in a standard activator-inhibitor reaction-diffusion model. Our model equations have four parameters governing local dynamics that are plausible targets of upstream regulation (Fig. 2C). Each parameter represents a distinct mechanism through which a

regulator could influence the formation of parallel stripes, and each one can theoretically be modulated by a spatial gradient. By directly simulating these equations, the specific effect of any gradient on pattern formation can be tested. To this end, we used spectral numerical techniques to perform exhaustive numerical screens to explore the effects of a wide range of plausible regulator profiles, both monotonic and multi-peaked.

To specifically investigate how well a given upstream modulator can steer the activator-inhibitor system into producing the parallel stripe pattern observed in striped mice, we performed four computational screens, one for each parameter, in which we simulated pattern formation for a sequence of ~40,000 different modulator distributions (see STAR Methods) to find distributions which replicated a pattern consistent with the observed pattern *in vivo* (Fig. 2D, E). Optimal regulator patterns were selected from a test set (Supplemental Movie 1) that produced final patterns scored as having a high similarity to the stripe pattern of placode formation seen in striped mice (Fig. 2E). Surprisingly, for three of the four potential pathways (μ, ρ, and ν), a simple dorsoventral gradient was the most consistent distribution to robustly produce localized, simulated peaks in a stripe-like manner. It is important to note that, while this is the simplest solution computationally, in nature there are likely to be multiple reinforcing, partially redundant mechanisms to assure robustness. However, our computational analysis strongly implies that a dorsoventral orienting gradient can control establishment of the striped pattern.

Taken together, our transcriptomic experiments coupled to our mathematical simulation data suggest that *Sfrp2*, a gene expressed in a dorsoventral gradient at a stage coinciding with the

emergence of embryonic placodes, may control the pattern of placode formation seen in striped mice.

Sfrp2 expression correlates negatively with Wnt signaling

Sfrp2 is a known soluble modulator of Wnt signaling, having dual roles as both an activator and repressor, depending on cellular microenvironment (Kim et al., 2016; Liang et al., 2019; Lin et al., 2016; van Loon et al., 2021). To uncover the relationship between *Sfrp2* and Wnt signaling in striped mouse skin, we dissociated dorsal skin from regions R1, R2, and R3 of E16.5 embryos, as before, and performed single-cell 3' - RNA-sequencing (scRNA-seq, 10X Genomics). We combined an equal number of cells from R1-R3 to generate a single pool representative of striped mouse E16.5 dorsal skin and identified fourteen distinct cell types based on expression of known molecular markers (Fig. 3A, Table S2) (Gupta et al., 2019; Rezza et al., 2016; Sennett et al., 2015). *Sfrp2* was specifically expressed in a subset of dermal fibroblasts, as judged by co-localization with canonical fibroblast markers (Fig. 3B, Table S2). Next, we clustered cells based on *Sfrp2* expression to define a population of *Sfrp2*-high (i.e., > 2UMIs) and *Sfrp2*-low (i.e., < 2 UMIs) fibroblasts (Fig. 3C). Differential gene expression analysis between *Sfrp2*-high and *Sfrp2*-low cells yielded numerous genes (P_{adj} <0.05), 482 of which were upregulated and 272 that were downregulated in *Sfrp2*-high compared to *Sfrp2*-low cells (Table S3). Among the genes

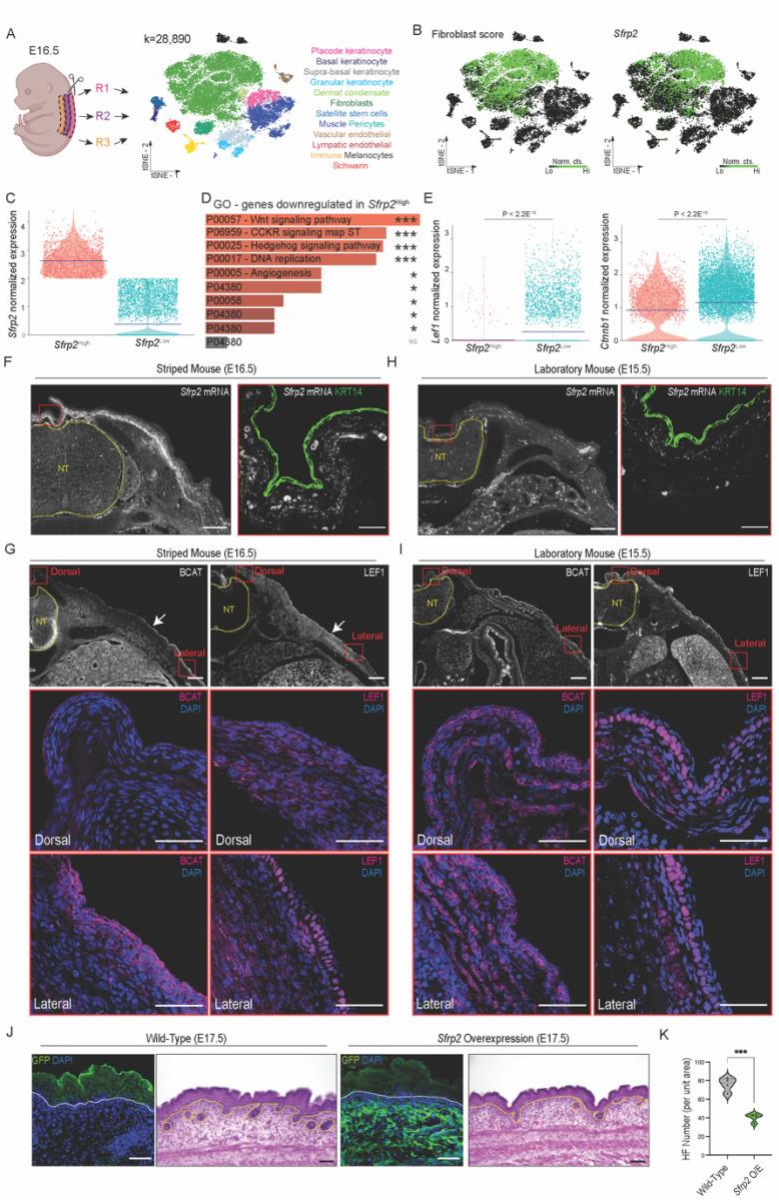

Figure 3. Relationship between *Sfrp2* and Wnt signaling in striped mouse's embryonic skin. (A) Schematic of a striped mouse E16.5 embryo highlighting dorsal skin regions (R1-R3) dissected for scRNA-seq (left) and clustering of skin cell types based on their gene expression profiles (right). (B) Cells in green correspond to dermal fibroblasts, as determined by their high fibroblast score (left, see STAR Methods). *Sfrp2* expressing cells cluster with a subset of dermal fibroblast cells (right). (C) Fibroblasts clustered based on high (> 2 UMI) and low (< 2 UMI) *Sfrp2* expression. (D) Ontology analysis for genes that are downregulated in *Sfrp2* low cells, showing Wnt signaling as one of the main enriched pathways (Enrichr, $P_{adj} < 0.05$). (E) Expression levels for markers of canonical Wnt signaling, *Lef1* and *Ctnnb1*, show upregulation in *Sfrp2* low cells (non-parametric Wilcoxon Rank Sum test). (F-H*) In situ* hybridization for *Sfrp2* coupled with immunofluorescence for the keratin marker KRT14 showing differences in dermal *Sfrp2* expression between stage-matched striped mouse (F) and laboratory mouse (H) embryos. (G-I) Immunofluorescence for CTNNB1 and LEF1 in the developing skin of stage-matched striped mouse (G) and laboratory mouse (I) embryos. Red boxes denote zoomed-in regions of dorsal and lateral skin. (J) Representative GFP and Hematoxylin-Eosin (H&E) stained transverse sections showing, respectively, the distribution of SFRP2 and hair follicles in control and transgenic mice. (K) Quantification of hair follicle number in transgenic mice and controls (N = 4; *** P < 0.001). Dotted lines in (J) delineate the dermis-epidermis boundary. Scale bars: 200µm (zoomed out) and 25µm (zoomed in) in (F and H); 200µm (zoomed out) and 50µm (zoomed in) in (G and I); and 50µm in (J). NT = neural tube.

169

upregulated in *Sfrp2*-low fibroblasts, Gene Ontology analysis identified regulation of Wnt signaling as the most significantly enriched pathway (Fig. 3D). Indeed, expression of numerous Wnt-related genes, including key activators of the pathway (i.e., *Lef1* and *Ctnnb1*), were higher in *Sfrp2*-low (Fig. 3E, Table S3) compared to *Sfrp2*-high cells, demonstrating that *Sfrp2* and Wnt activation are negatively correlated in striped mice dermal fibroblasts.

To confirm and extend our previous observation, we examined spatial patterns of *Sfrp2* expression and Wnt signaling markers. RNA *in situ* hybridizations in cross sections from E16.5 striped mice embryos, coupled to immunohistochemistry (IHC) for an epidermal marker (KRT14), indicated that expression of *Sfrp2* was strong in mesenchymal cells directly above the neural tube and decreased laterally, a result consistent with our bulk-level RNA-seq analysis (Fig. 3F). At this same stage, immunofluorescence (IF) for LEF1 and CTNNB1 showed that these markers were readily detectable in epidermal cells from lateral and ventral regions of the embryo but were absent from cells above the neural tube and adjacent areas, where *Sfrp2* expression was highest (Fig. 3G). This pattern contrasted with what was seen in stage-matched laboratory mouse embryos (E15.5), which had overall lower levels of dermal *Sfrp2* expression (Fig. 3H) and uniform levels of LEF1 and CTNNB1 throughout the epidermis, including above the neural tube (Fig. 3I). Taken together, our scRNA-seq data coupled to RNA *in situ*/IF analysis indicate that *Sfrp2* and Wnt signaling are negatively correlated and suggest that dermal *Sfrp2* expression acts to inhibit Wnt signaling in striped mouse embryonic skin.

Sfrp2 overexpression alters placode formation in laboratory mice

Wnt signaling is a primary determinant of hair follicle formation and spacing, as perturbation of members of this pathway leads to alterations in hair follicle number and distribution (Andl et al., 2002; Gat et al., 1998; Millar, 2002; Tsai et al., 2014). This raises the intriguing hypothesis that *Sfrp2* may be acting to directly regulate striped mouse placode development. If this is the case, one would predict that increasing expression of *Sfrp2* in embryonic skin with low endogenous levels of *Sfrp2*, such as that of laboratory mouse (Rezza et al., 2016; Sennett et al., 2015), should alter placode formation. To test this, we generated $Rosa^{Sfrp2\text{-}GFP}$ mice, a strain that allowed us to activate *Sfrp2* transcription in the presence of tissue-specific Cre drivers. To establish whether dermal expression of *Sfrp2* was sufficient to regulate placode formation, as implied by our striped mouse data, we crossed $Rosa^{Sfrp2\text{-}GFP}$ mice with *Dermo-Cre* mice, a mesenchymal driver of Cre (Šošić et al., 2003; Yu et al., 2003) (Fig. 3J). Indeed, double-transgenic embryos (*Dermo-Cre*;$Rosa^{Sfrp2\text{-}GFP}$) analyzed at E17.5 showed a significant reduction in the number of placodes/hair follicles, compared to control littermates (N= 4) (Fig. 3J, K). Thus, our transgenic experiments in laboratory mice demonstrate a functional relationship between *Sfrp2* and embryonic placode development in which elevated levels of *Sfrp2* in the dermis leads to a marked reduction in the number of placodes/hair follicles.

The establishment of the _Sfrp2_ dorsoventral gradient

In striped mice, *Sfrp2* is expressed in a dorsoventral gradient at E16.5, a stage coinciding with the emergence of embryonic placodes. To understand how such a pattern is established in space and time, we characterized the expression dynamics of *Sfrp2* by performing additional scRNA-seq analysis from the days prior to E16.5 (Fig. 4A). We found that the number of fibroblasts

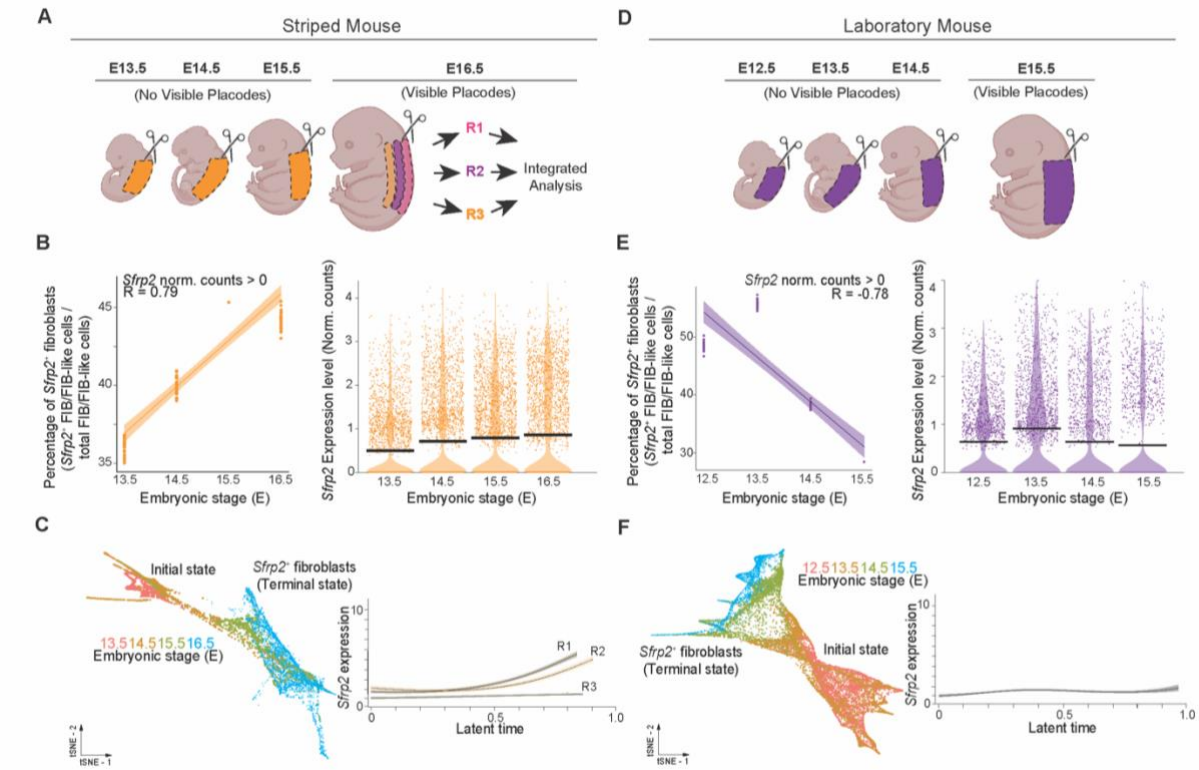

Figure 4. Spatial and temporal Sfrp2 expression patterns in striped mice and lab mice. (A) Schematic of striped mouse skin dissections from different developmental stages. For E16.5, scRNA-seq was performed on each individual region and data were pooled for an integrated analysis representative of whole striped mouse dorsal skin. (B) Both the percentage of fibroblasts that express *Sfrp2* (left, Spearman's Correlation, R = 0.79) and the expression levels of *Sfrp2* within those fibroblasts (right) increase in the days prior to visible placode formation in striped mouse dorsal skin. (C) Developmental trajectories inferred from striped mouse fibroblasts show regional differences in *Sfrp2* expression in latent time. (D) Schematic of laboratory mouse dissections from different developmental stages used for scRNA-seq. For all stages (E12.5-E15.5), whole dorsal skin was dissected (purple). (E) Both the percentage of fibroblasts expressing *Sfrp2* (left, Spearman's correlation, R = -0.78) and *Sfrp2* expression levels within those fibroblasts (right) decrease in the days prior to visible placode formation. (F) Developmental trajectories inferred from laboratory mouse fibroblasts show no substantial change in *Sfrp2* expression in latent time. Black lines in (B) and (E) indicate mean *Sfrp2* expression levels.

expressing *Sfrp2* was lowest at the earliest time-point sampled, E13.5 (36.03%), and gradually increased in subsequent days (40.03% at E14.5, 45.34% at E15.5, and 44.23% at E16.5) (Spearman correlation=0.79) (Fig. 4B). Moreover, average *Sfrp2* expression levels within those fibroblasts also increased during this period (Fig. 4B). In agreement with these observations, we observed a marked change in *Sfrp2* expression in a developmental trajectory of dermal fibroblasts modeled in latent time. Specifically, *Sfrp2* exhibited a prominent spatiotemporal increase across development toward R1-R3 regions at E16.5, having higher levels of expression

in the region closest to the dorsal midline relative to the more lateral regions (*i.e.*, R1>R2 and R2>R3) (Fig. 4C).

We next asked whether the sharp increase in *Sfrp2* expression prior to placode formation was a unique feature of striped mice or, instead, a conserved process in rodent skin development. To address this, we performed scRNA-seq on laboratory mouse dorsal skin from multiple stages, including those preceding placode formation as well as at stages when placodes have formed (E12.5-E15.5) (Fig. 4D). In stark contrast to what was observed in striped mice, we found that the percentage of *Sfrp2*-expressing fibroblasts was highest early on (48.44% at E12.5) and decreased in subsequent days (28.44% at E15.5) (Spearman correlation=-0.78). In addition, average *Sfrp2* expression levels within fibroblasts also decreased from E13.5-E15.5 (Fig. 4E). Lastly, contrary to what we found in striped mice, *Sfrp2* expression levels in laboratory mice fibroblasts showed no substantial change in latent time (Fig. 4F).

Together, our results indicate that *Sfrp2* levels in the dorsal mesenchyme of striped mice gradually increase prior to placodes becoming visible and reach peak numbers at the onset of placode formation. In line with our mathematical model and transgenic experiments, increased *Sfrp2* levels are sufficient to modulate the underlying developmental program controlling hair follicle formation. Moreover, our comparative analysis reveals opposing dynamics in laboratory mice, where *Sfrp2* expression levels decrease as placode formation nears, thereby allowing this process to proceed uniformly across the dorsal skin.

Sfrp2 shifts in spatial expression and regulates pigmentation by activating Wnt signaling

Our phenotypic characterization of striped mouse embryonic skin shows that, at E18.5, placodes become visible in regions where they were previously absent (Fig. S2). We reasoned that if *Sfrp2* indeed contributes to establishing patterns of placode formation in stripe mice, as our data suggest, there should be a detectable change in the spatial expression of this gene once placodes emerge throughout the dorsal skin. To test this, we characterized the spatial-specific patterns of *Sfrp2* expression in late embryogenesis (E19.5) and early postnatal stages (P0 and P4) using qPCR. For all samples, we dissected three different skin regions (R1-R3) using either hair-length (E19.5) or visible pigmentation differences (P0 and P4) as a proxy for defining region boundaries and isolating tissue (Mallarino et al., 2016) (Fig. 1D). In agreement with our prediction, we found no regional differences in *Sfrp2* levels at E19.5, demonstrating there had been a shift in the spatial expression pattern of this gene and that the dorsoventral gradient seen at E16.5 was no longer present (Fig. 5A). Unexpectedly however, when we analyzed skin regions from pups (P4), we found that *Sfrp2* had undergone an additional shift in its spatial pattern and was now expressed at significantly lower levels in the light stripes (R2) compared to the flanking dark stripes (R1 and R3) (Fig. 5A). The light-stripe specific decrease in *Sfrp2* expression seen in P4 pups suggested this gene could be playing an additional role in striped mouse skin, regulating hair color during the period in which pigment is synthesized and deposited in the growing hair shaft. Furthermore, previous studies have shown that pigment production/melanogenesis can be controlled by Wnt signals secreted from the dermal papilla (Enshell-Seijffers et al., 2010; Morgan, 2014), a specialized mesenchymal component of the hair follicle that signals to pigment-producing cells, or melanocytes. To explore a potential link between *Sfrp2* and melanogenesis, we first performed fluorescent *in situ* hybridizations on P4

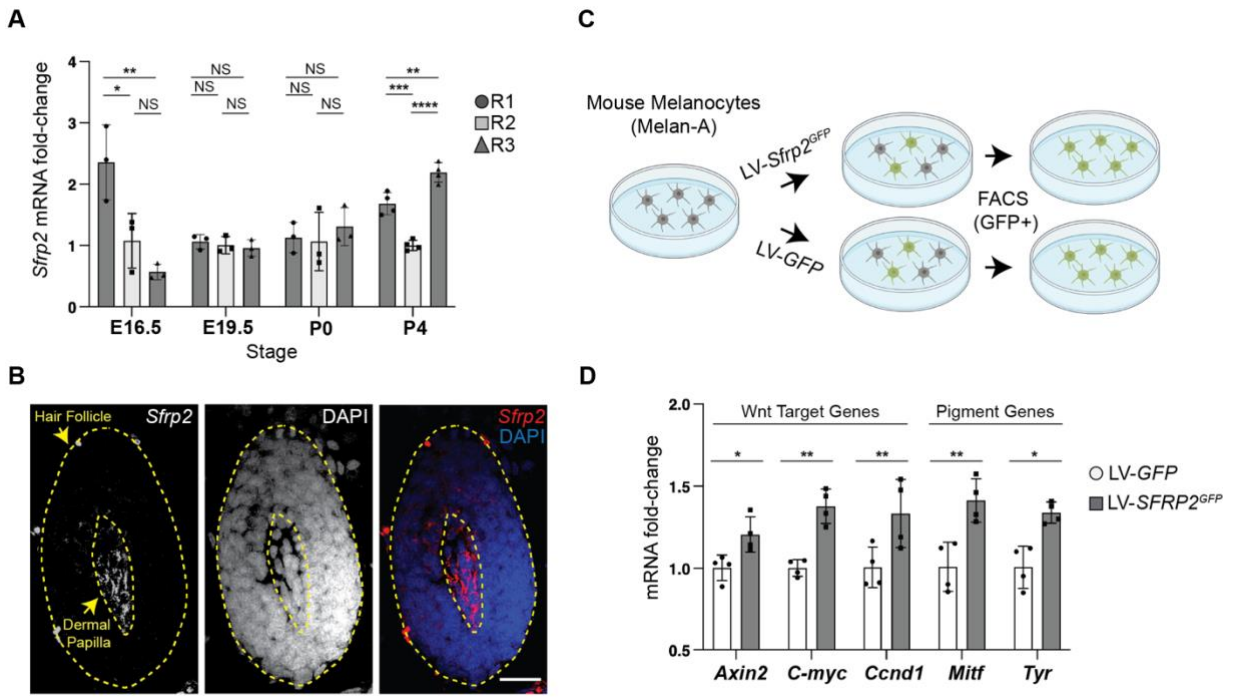

Figure 5. *Sfrp2* promotes melanogenesis by activating Wnt signaling. (A) Quantitative PCR (qPCR) showing *Sfrp2* mRNA fold change levels along different dorsal skin regions in embryonic and postnatal stages. (B) *In situ* hybridization showing specific *Sfrp2* expression in the dermal papilla of a P4 striped mouse hair follicle. (C-D) Functional *in vitro* experiments using lentiviruses. (C) Schematic of the design of *in vitro* functional experiments. Melanocytes were stably transduced with either a control (LV-*GFP*) or an experimental (LV-*Sfrp2*^{GFP}) lentivirus and sorted using FACS. (D) Fold change differences in expression of Wnt targets and melanogenesis genes in stably transduced control and experimental cells, as determined via qPCR. Statistical significance in panel (A) (**** P < 0.0001; *** P < 0.001; ** P < 0.01; *P < 0.05, N = 3 for E16.5, E19.5, and P0, N = 4 for P4) and in panel (D) (** P < 0.01; *P < 0.05; N = 4) was assessed using an ANOVA test.

striped mouse skin sections and found that *Sfrp2* was specifically expressed in the dermal papilla (Fig. 5B), a pattern consistent with what is seen in laboratory mouse (Rezza et al., 2016; Sennett et al., 2015) and with our hypothesis that this gene may regulate melanogenesis. Next, to test the effect of *Sfrp2* expression on melanocyte behavior, we stably transduced an immortalized mouse melanocyte cell line (Melan-A) with a lentiviral vector carrying the *Sfrp2* cDNA and used qPCR to measure the expression of Wnt targets and of genes involved in melanogenesis (Fig. 5C, D). Compared to melanocytes transduced with a control virus, cells overexpressing *Sfrp2* showed a significant increase in Wnt target genes, including *Axin2*, *C-myc*, and *Ccnd1* (He et al., 1998; Jho et al., 2002; Shtutman et al., 1999). Moreover, relative to controls, cells overexpressing *Sfrp2*

showed a marked increase in *Tyr* and *Mitf*, two genes with key roles in promoting melanin synthesis (Iozumi et al., 1993; Steingrímsson et al., 2004) (Fig 5D). Notably, these results are consistent with previous findings, in which recombinant SFRP2 was found to activate Wnt/melanogenesis in human primary melanocytes via paracrine signaling and to promote darkening of skin explants (Kim et al., 2016).

Taken together, our results indicate that the expression pattern of *Sfrp2* during embryogenesis and early postnatal stages is dynamic, shifting from a 'high-low', dorsoventral gradient (E16.5) to a 'high-low-high' pattern (P4) in which regions of low expression (i.e., light stripes) are flanked by regions where expression is higher (i.e., dark stripes). Moreover, our spatial expression data and *in vitro* functional experiments indicate that postnatal expression of *Sfrp2* acts to regulate melanocyte behavior via Wnt activation, thereby revealing an additional regulatory function for *Sfrp2* during stripe pattern formation.

Sfrp2 in vivo knockout in striped mice leads to changes in coat pattern and pigmentation

Our data implicate *Sfrp2* as a key regulator of striped mouse placode formation and stripe-specific pigmentation differences. However, to establish a direct causal link between *Sfrp2* and coat pattern phenotypes, it is critical to perform functional experiments directly in striped mice. To this end, we adapted a CRISPR-based experimental strategy in which recombinant adeno-associated viruses (rAAVs) are used to deliver CRISPR-CAS9 reagent into the oviduct of pregnant females. This *in vivo* gene editing technique is based on the ability of rAAVs to transduce the zona pellucida on intact pre-implantation embryos (Yoon et al., 2018) (Fig. 6A). First, to establish the feasibility of using this approach for inducing gene knockouts (KO) in

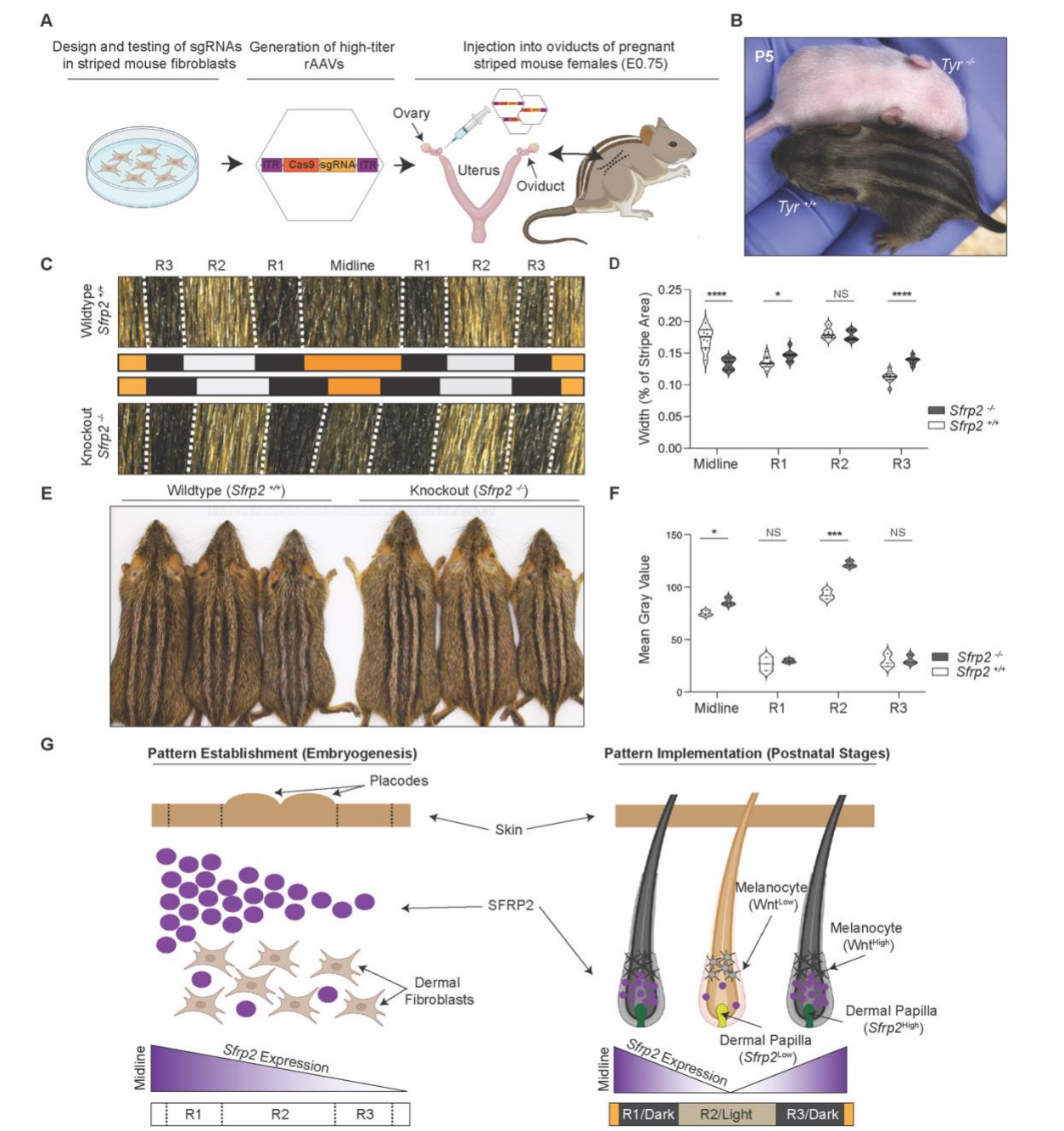

Figure 6. *In vivo* genome editing in African striped mice. (A) Schematic of the CRISPR-based approach used for generating targeted genome deletions in the striped mouse. (B) Postnatal Day 5 (P5) striped mouse littermates showing differences between a Tyrosinase (Tyr) wildtype individual ($Tyr^{+/+}$) and a knockout animal ($Tyr^{-/-}$) (C-D) Sfrp2 regulates stripe pattern width. (C) Representative differences in stripe width seen between wildtype ($Sfrp2^{+/+}$) controls and Sfrp2 knockout ($Sfrp2^{-/-}$) pups. (D) Measurements of stripe width in $Sfrp2^{+/+}$ and $Sfrp2^{-/-}$ pups. Statistical significance in panel (D) (**** $P < 0.0001$; *** $P < 0.001$; ** $P < 0.01$; *$P < 0.05$; $Sfrp2^{+/+}$, N = 10; $Sfrp2^{-/-}$, N = 7) was assessed using an ANOVA test. (E) Representative differences in coat color between $Sfrp2^{+/+}$ and $Sfrp2^{-/-}$ adult mice taken as a single image. (F) Quantification of pigmentation between $Sfrp2^{+/+}$ and $Sfrp2^{-/-}$ adult mice reveal stripe-specific changes in color. Statistical significance in panel (F) (*** $P < 0.001$; *$P < 0.05$; $Sfrp2^{+/+}$, N = 3; $Sfrp2^{-/-}$, N = 3) (G) Model describing the role of Sfrp2 in establishing and implementing the stripe color pattern in striped mice.

striped mice *in vivo*, we injected pregnant females carrying pre-implantation embryos with an rAAV packaged with Nme2Cas9 and a single-guide RNA (sgRNA) expression cassettes directed to the coding sequence of *Tyrosinase* (*Tyr*), the rate limiting enzyme for melanin production (Edraki et al., 2019; Iozumi et al., 1993). Visual inspection of F0 pups coupled to genotyping revealed this approach resulted in efficient gene editing, enabling us to generate complete KO animals (Fig. 6B). To our knowledge, this is the first time that *in vivo* gene editing has been performed in a mammalian species outside of laboratory mouse.

Encouraged by our proof-of-principle results, we next designed multiple sgRNA's against the 5' coding region of *Sfrp2* (Fig. S4A; STAR Methods). We then tested each sgRNA in striped mouse immortalized dermal fibroblasts and chose the one that had the highest indel-inducing efficiency. Next, we injected an rAAV containing Nme2Cas9 and sg*Sfrp2* expression cassettes into the oviducts of plugged females. From a total of 21 females injected, we obtained 57 pups, 14 of which carried gene edits in *Sfrp2*. After mating F0 founders and wildtype animals ($Sfrp2^{+/+}$) to ensure germline transmission, we crossed F1 heterozygous animals ($Sfrp2^{+/-}$) to generate F2 *Sfrp2* KO ($Sfrp2^{-/-}$) mice. We used western blot to confirm the successful elimination of SFRP2 protein (Fig. S4B). Analysis of coat phenotypes from early postnatal (P3) stages revealed significant and consistent differences in the coat patterns of F2 $Sfrp2^{-/-}$ and $Sfrp2^{+/+}$ striped mice. Specifically, while the width of the striped area (i.e., the distance between both R3 stripes on either side of the midline) remained the same, we observed significant changes in the relative width of the stripes, with $Sfrp2^{-/-}$ mice having a narrower middle stripe and wider dark stripes than $Sfrp2^{+/+}$ mice (Fig. 6C, D). Thus, deletion of *Sfrp2* induces significant alterations in the stripe boundaries within the striped area, effectively altering the stripe pattern. In addition to

the changes in the stripe pattern, analysis of coat coloration in adults, when pigment deposition has been completed, revealed that the coats of *Sfrp2*$^{-/-}$ mice were lighter than *Sfrp2*$^{+/+}$ mice (Fig. 6E). Such difference was particularly evident in regions with light/banded hair (e.g., middle stripe and light stripes), as determined by quantitative measurements taken from photographs (Fig. 6F).

The stereotyped coat pattern of striped mice likely results from multiple, reinforcing mechanisms and, thus, knockout of a single gene is not expected to completely abrogate the pattern (see Discussion). However, our genome editing experiments in striped mice demonstrate a key role for *Sfrp2* in regulating both pigment distribution (i.e., color pattern) and pigment type (i.e., overall color) in this species.

Discussion

Over the course of millions of years of evolution, the skin developmental program has been altered many times to produce a stunning array of phenotypic diversity that is apparent from comparisons both across species and within the body of a single individual. Here, by taking advantage of naturally evolved phenotypic variation in striped mouse, a species that we have now transformed into a genetically tractable laboratory model, we studied the developmental processes involved in regulating periodic stripe patterns. During mid embryogenesis, striped mouse placodes emerge in a spatially restricted way, foreshadowing the coat pigment pattern visible in early postnatal days. Embryonic regions where placodes initially fail to form give rise to dark colored stripes, implying that a molecular pre-pattern is established either simultaneously or prior to placode formation. Once this pre-pattern is established, cells in placode barren skin

regions acquire permanent changes that are then relayed to hair follicle signaling centers during pigment production, or the implementation of the pre-pattern.

In birds and mammals, periodic pigment patterns arise from two sequential processes: the first occurs early in embryogenesis and specifies the positional boundaries of the future pattern (*i.e., pattern establishment, or prepattern*); the second implements this prepattern through genes mediating pigment production during hair growth and cycling, giving rise to the observed color differences (*i.e., pattern implementation*) (Haupaix and Manceau, 2020; Kaelin and Barsh, 2013). We identify *Sfrp2* as a regulator of both the establishment of the pre-pattern and its implementation, a dual role that is made possible by its dynamic expression pattern throughout embryogenesis and early postnatal stages (Fig. 6G). Prior to placode formation, expression levels of *Sfrp2* gradually increase in dorsal dermal fibroblasts, as does the number of *Sfrp2* expressing dermal fibroblasts. When placodes become visible, *Sfrp2* is expressed in a sharp dorsoventral gradient, with maximum levels in cells above the neural tube. Our simulations coupled to our transgenic experiments in both laboratory mice and striped mice show that the *Sfrp2* dorsoventral gradient can act to influence placode formation. Late in embryogenesis, the *Sfrp2* dorsoventral expression gradient disappears and placodes form throughout the dorsal skin. Then, at early postnatal stages, *Sfrp2* becomes differentially expressed in the dermal papilla of light and dark stripe hair follicles, where it acts to regulate melanocyte behavior. These results contrast with what is seen in felids, where the molecular players regulating pattern establishment are different from the ones controlling the implementation events that follow (Eizirik et al., 2010; Kaelin et al., 2012, 2021). The involvement of *Sfrp2* at multiple stages of pattern formation implies a fine-

tuned spatiotemporal regulatory control, likely achieved through a complex *cis*-regulatory architecture and the action of multiple binding factors (Keller et al., 2020).

Secreted frizzled-related proteins (SFRPs) are known modulators of Wnt signaling that can exert their effects through a wide variety of mechanisms, including Wnt ligand sequestering, binding to Frizzled receptors, stabilization of Wnt-Frizzled complexes, and direct activation of Frizzled (van Loon et al., 2021). As such, SFRPs can either inhibit or activate Wnt signaling, and their effect is dependent on cell type, developmental stage, and cellular microenvironment(van Loon et al., 2021). In striped mice, embryonic expression of *Sfrp2* in a subset of dermal fibroblasts causes a decrease of epidermal CTNNB1 and LEF1, leading to alterations in placode number. Later in development, dermal papilla-specific expression of *Sfrp2* alters melanocyte behavior, causing an increase in the expression of Wnt targets and genes involved in melanogenesis. Thus, our results show that *Sfrp2* can lead to opposing modulation (i.e., activation and inhibition) of Wnt signaling within the same tissue. Future dissection of the downstream pathways by which *Sfrp2* acts to respectively inhibit and activate Wnt signaling during placode formation and melanogenesis will reveal key insights into the precise mechanisms by which such opposing effects are achieved.

It is noteworthy that elimination of *Sfrp2* led to a subtle, albeit consistent difference in both the pattern and overall coat coloration of striped mice. This result can be explained by different factors, including the overall effect size of *Sfrp2* as well as possible redundancy and/or compensation with other molecules within the Wnt pathway and/or other pathways. For example, with respect to placode formation, our bulk-level RNA-seq data from E16.5 embryos shows that

there are additional Wnt inhibitors expressed at higher levels in R1 than in R4, including known repressors of placode formation such as *Dkk2* (Song et al., 2018). It is likely that such molecules act in coordination with *Sfrp2* to specify patterns of placode morphogenesis and are therefore still playing a substantial role in regulating this trait in *Sfrp2*$^{-/-}$ striped mice. Similarly, our previous work on pigmentation showed that hair color differences in striped mice are controlled by the interplay of melanocyte-autonomous (e.g., *Alx3*-mediated suppression of melanocyte differentiation) and non-autonomous processes (e.g., regulation of pigment-type switching by paracrine factors secreted from the dermal papilla, including *Asip* and *Edn3*) (Mallarino et al., 2016; Morgan, 2014). Thus, although *Sfrp2* influences pigmentation, as our experiments show, it is clear that modulation of hair color in striped mice is achieved through the combinatorial effect of multiple genes (Mallarino et al., 2016).

Stripe patterns have independently evolved multiple times among rodents, and different species display marked variation in both number of stripes and their position along the dorsoventral axis (Johnson et al., 2019). In agreement with our mathematical simulations, the ability of external gradients to robustly enforce simple parallel stripe patterns is well established as a generic mechanism in the theory of pattern formation (Hiscock and Megason, 2015). At the same time, because this mechanism works through selection of just a single spatial wavelength, it does not account for more complex patterns, which typically feature variations over several length scales simultaneously. Thus, while the *Sfrp2* dorsoventral gradient can account for the pattern seen in striped mice, the coat patterns of other rodents, such as those seen in the thirteen-lined ground squirrel (*Ictidomys tridecemlineatus*) or the zebra mouse (*Lemniscomys barbarus*), are likely generated through modifications of this mechanism or entirely different molecular processes.

In addition to the pigment stripes found in striped mice and other taxa (Bailleul et al., 2019; Haupaix et al., 2018; Kuriyama and Hasegawa, 2017; Murakami et al., 2018; Parichy, 2003), parallel stripe patterns are commonly seen in other tissues during animal development. In a companion paper, Kingsley et al report that the parallel orientation of the cartilage rings in the developing chick airway is generated through the interplay of a Turing-like mechanism and an orienting dorsoventral gradient of SHH. Thus, it is likely that interacting signaling gradients and Turing systems represent a widespread mechanism for generating stripe-like patterns in multiple tissues and shaping animals during embryogenesis.

By integrating multidisciplinary approaches, our work reveals insights into the mechanisms by which spatial patterns are established in developing embryos. In addition, by extending *in vivo* genome editing approaches to striped mice, a technique previously restricted to traditional mammalian laboratory models (i.e., laboratory mouse), our work exemplifies the potential of using emerging model species to uncover the mechanistic basis of naturally evolved phenotypic traits and will open the door for functional studies in other mammals.

Acknowledgements

We thank members of the Mallarino lab; Princeton LAR (Chris Dmytrow, Kirsten Gerhart, Grace Barnett, and Jamus McGuire) for help with striped mice husbandry; the LSI Genomics Core (Wei Wang, Jennifer M. Miller, Jessica Wiggins, and Jean Arley Volmar) for help with library preparation and sequencing; the Nikon Center of Excellence Confocal Microscopy Core (Gary Laevsky, Sha Wang); and members of the Rivera-Perez lab (Yeonsoo Yoon and Judith

Gallant) for help with *in vivo* genome editing experiments. We also thank Eric F. Wieschaus and Ghirish Deshpande for insights and discussion.

Author contributions

MRJ and RM conceived the project and designed experiments. MRJ performed all RNA sequencing experiments and bulk RNA sequencing analysis. CFG-J led the scRNAseq analysis, with support from MRJ and QN. SL performed the *in vitro* and *in vivo* genome editing in striped mice, with help from JAR-P and SAM. MRJ and SL performed all downstream processing and analysis of genome edited animals. MRJ and RM performed *in situ* hybridizations. PM and SYS did the mathematical modeling. MRJ, SAM, and BB performed the phenotypic characterization of striped mouse and laboratory mouse tissues, including immunofluorescence and histology. MRJ and SAM performed the melanocyte cell culture experiments. CF generated the "*Rhabdomyzed" Mus* genome and Liftover annotation. JG and AP generated the immortalized *Rhabdomys* fibroblasts. MRJ and RM wrote the manuscript with input from all authors.

Funding

This project was supported by an NIH grant to RM (R35GM133758). MRJ was supported by an NIH fellowship (F32 GM139253). SL was supported by a Presidential Postdoctoral Research fellowship (Princeton University). BB was supported by an NIH training grant (T32GM007388). CF was supported by an NIH fellowship (F32 GM139240-01). C.F.G-J. is partially supported by UC Irvine Chancellor's ADVANCE Postdoctoral Fellowship Program. QN was partially supported by an NSF grant DMS1763272 and a Simons Foundation grant (594598).

Competing interests

The authors of this publication declare that they have no competing interests.

Data and materials availability

The bulk RNA-seq and scRNA-seq reads are submitted under NCBI BioProject: XYZ.

Methods

Striped mouse husbandry

F10 descendants of wild-derived striped mice (*Rhabdomys pumilio)*, originating from Goegap Nature Reserve, South Africa, S 29° 41.56′, E 18° 1.60′, were originally obtained from a captive colony at the University of Zurich (Switzerland) and are maintained at Princeton University. *R. pumilio* are kept at a 16:8 light-dark cycle and given food *ad libitum*. All experiments performed were approved by Princeton University's Institutional Animal Care and Use Committee.

Embryo staging

To create a developmental timeseries of striped mouse embryonic development, embryos spanning mid-gestation were collected and ordered chronologically, based on embryo size and various morphological features including eye pigmentation, webbing of the forelimb and hindlimb, and skull morphology (Kaufman, 1992). The stage at which epidermal hair placodes first become visible in striped mice was considered "stage matched" to *Mus* E15.5, the stage at which hair placodes first become visible by eye in *Mus*. Indeed, other morphological features in striped mice at this stage agreed remarkably well with that of E15.5 laboratory mouse embryos. This stage in striped mice was later confirmed to be E16.5 via a combination of vaginal cytology and ultrasound imaging. Staging of all striped mouse embryos was confirmed using vaginal cytology and ultrasound imaging.

Sample preparation for *in situ* hybridization and immunofluorescence

Pregnant females of the appropriate stage were euthanized following approved protocols. Embryos were harvested, fixed in 4% paraformaldehyde (PFA), dehydrated in increasing concentrations of Methanol/PBS (25%, 50%, 75%, and 100%), and stored at -20°C. For whole-mount *in situ* hybridizations, embryos were rehydrated in decreasing concentrations of Methanol/PBT (75%, 50%, and 25%), and washed with PBS. For section *in situ* hybridizations and immunofluorescence, embryos were rehydrated as described above and then incubated in 10% sucrose overnight (O/N) at 4°C, followed by a 30% sucrose O/N incubation at 4°C. Embryos were then incubated in 50% Sucrose, 50% OCT (optimal cutting temperature) compound for 3 hours at room temperature, embedded in OCT, flash frozen, and cryosectioned (16um thickness) using a Leica CM3050S Cryostat. Slides were frozen at -80°C until use.

Whole Mount *in situ* hybridizations

mRNA sequences for target genes were obtained either from NCBI (*Mus musculus*) or a denovo transcriptome (*R. pumilio*) (Mallarino et al., 2016). For *R. pumilio*, we generated the following anti-sense riboprobes: *Dkk4* (543bp), *Wif1* (563bp), *Bmp4* (619bp), *Wnt10b* (360bp), *Dkk1* (546bp), and *Ctnnb1* (400bp). For *M. musculus*, we generated a *Dkk4* probe (550bp). All primer sequences are reported in Table S4. All probes were sequence-confirmed using Sanger Sequencing. Whole-mount *in situ* hybridizations were then performed using previously described protocols(Wu and Wang, 2019). Briefly, embryos were post-fixed with 4% PFA in PBS, washed with PBS, treated with 20ug/mL proteinase in PBT for 45 min, and incubated O/N with riboprobes at 65°C. The following morning, probes were washed with MABT (Maleic acid, NaCl, Tween-20) and incubated O/N with secondary anti-DIG antibody (1:2000) diluted in

MABT, 2% Boehringer Blocking Reagent, and 20% heat-treated sheep serum. After washing several times with MABT, the signal was developed by incubating with NBT/BCIP. Once signal had developed sufficiently, the reaction was stopped by washing several times with PBT and fixing in 4% PFA O/N. Embryos were visualized using a SMZ18 stereo microscope (Nikon). At least 3 embryos per probe per species were analyzed.

Bulk-level RNA sequencing

E16.5 striped mouse embryos (N = 3) were harvested from pregnant females and placed in 1x PBS on ice. Regions R1 (dorsalmost, placode barren), R2 (dorsalmost, placode rich), R3 (ventralmost, placode barren), and R4 (ventralmost, placode rich) were micro-dissected using morphological placodes as reference points. Regions from both sides of the midline were combined into a single tube containing 500ul of RNALater (Invitrogen) and stored at -20°C until RNA extraction. RNA was extracted using the RNeasy fibrous tissue mini kit (QIAGEN) per the manufacturer's protocol. RNA-sequencing libraries were prepped using the TruSeq RNA Library Prep kit v2 (Illumina) and sequenced on a NovaSeq 6000 (2 x 65bp, paired-end). Pairwise differential expression analyses between the transcriptomes of dorsal skin regions R1-R4 were performed using DeSeq2 v1.30.1 from BioConductor (https://bioconductor.org/) (Michael I Love, Wolfgang Huber, Simon Anders, 2014) . Only genes differentially expressed with an adjusted p-value < 0.05 were considered. For visualization of all comparisons simultaneously, UpSet plots were generated using Upset R (Conway et al., 2017).

Modeling stripe patterns of placode formation

Model Preliminaries

We modeled the pattern forming process using a variant of the classical Gierer-Meinhardt (GM) model of the Turing mechanism (Gierer and Meinhardt, 1972). This two-species activator-inhibitor model is an archetypal model of stripe and spot formation in biological systems, and its behavior with respect to pre-existing spatial gradients has been extensively studied (Van Gorder, 2021). The use of this model is further justified by its previous success in reproducing follicle patterning in *M. musculus*(Sick et al., 2006). We use the following form of this model:

$$\partial_t u = D_u \partial_{xx} u + \frac{k_2 u^2}{(g + v)\left(1 + \frac{u^2}{k_3}\right)} - k_1 u$$

$$\partial_t v = D_v \partial_{xx} v + \frac{k_5 u^2}{\left(1 + \frac{u^2}{k_3}\right)} - k_4 v$$

defined on a 1D periodic domain $[-L, L]$. Note that $g \ll 1$ is a small regularizing term added to reduce numerical stiffness and will be neglected in our analysis. It is convenient for our analysis to shift to a non-dimensional version. We rescale our variables as $\overline{x} = \frac{x}{L}$, $\overline{t} = \frac{D_v t}{L^2}$, $\overline{u} = \frac{k_3 u}{k_2}$ and $\overline{v} = \frac{k_5 v}{k_2}$ for dimensionless variables $\bar{x}, \bar{t}, \bar{u}$, and $\bar{v}$. Under this transformation, after dropping the overbars for convenience, our model takes the form

$$\partial_t u = \delta^2 \partial_{xx} u + \frac{\rho\, u^2}{(\gamma + v)\left(1 + \frac{u^2}{K}\right)} - \mu u$$

$$\partial_t v = \partial_{xx} v + \frac{\rho\, u^2}{\left(1 + \frac{u^2}{K}\right)} - \nu v$$

with $\mathrm{K} = \frac{k_5^2 k_3}{k_2^2}$, $\rho = \frac{k_2 L^2}{D_v}$, $\mu = \frac{k_1 k_2}{k_5}$, $\nu = \frac{k_4 k_2}{k_5}$, $\gamma = \frac{k_5\, g}{k_3}$ and $\delta^2 = \frac{D_u}{D_v}$.

In this form, discounting diffusivity δ, there are four possible parameters which could represent the effect of an upstream regulator such as *Sfrp2*.

Stability and Pattern Formation

For correct choice of parameters, this system of equations exhibits a Turing instability and subsequent pattern formation. A full bifurcation analysis is outside the scope of this paper, and similar studies have been performed for several variants of the GM system (Song et al., 2017; Wei and Winter, 2014). However, we do highlight sufficient conditions for the system to be unstable to spatial perturbation: in the limit $\gamma \to 0$ there must exist some integer $n > 0$ such that one of two cases holds:

Case 1:

$$\mu > n^2\pi^2(1+\delta^2) + \nu \text{ and } K > \frac{\nu^2(n^2\pi^2(1+\delta^2)+\mu+\nu)}{\mu^2(-n^2\pi^2(1+\delta^2)+\mu-\nu)}$$

Case 2:

$$K > \frac{(n^2\pi^2\delta^2+\mu)\nu^2(n^2\pi^2+\nu)}{\mu^2(-n^4\pi^4\delta^2-\mu\nu+n^2\pi^2(\mu-\delta^2\nu))}, \nu < n^2\pi^2 \text{ and } \mu > \frac{n^2\pi^2\delta^2(n^2\pi^2+\nu)}{n^2\pi^2-\nu}.$$

Numerical analysis of upstream modulators

Suppose we choose some point in the Turing-unstable region of the parameter space, for example for the values listed in Table S5. Starting from random initial conditions, a pattern of peaks and valleys will spontaneously form as the system converges to a steady state. This steady state is typically not very robust: pick a slightly different initial condition and peaks will form at different places and possibly in different numbers. To robustly place peaks where we want them

to go, we proposed to take this random pattern forming state and control it by introducing a spatially varying regulator. We assume that this regulator exists over the entire domain and serves to modify local chemical kinetics. These kinetics are wholly controlled by the four parameters $\mu, \nu, \rho,$ and K, so, to systematically examine possible modulations, we explore the effect of coupling each parameter in turn to a spatially varying, temporally constant field (e.g., $\mu \rightarrow \mu(x) = \mu \cdot S(x)$). Modern spectral integration methods, in combination with elementary parallelization, have made it computationally cheap to simulate equation systems like ours: it is feasible to aggressively sample a large function space of possible prepatterns. Our basic methodology, then, is to choose to repeatedly modulate each parameter according to different choices of $S(x)$, leaving the other parameters fixed, and observing what patterns emerge consequently. We ask, for each parameter, what choice of $S(x)$ guides the reaction diffusion equations to the best fit to an empirically derived stripe spacing. This function belongs to the following family of functions

$$S_{C_i}(x) = \sum_{i=1}^{12} C_i \, T_{2i}(x)$$

Here, $T_n(x)$ is the nth Chebyshev polynomial, making $S(x)$ an element of a twelve-dimensional function space specified by the amplitudes C_i. The cap of $n = 12$ was chosen under the assumption that the prepattern should not have a substantially finer spatial structure than the downstream pattern. The characteristic diffusion scale of the above system is $1/\sqrt{\nu} = 0.1$, so we chose an upper mode with a length scale somewhat smaller than this to ensure we could cover a large set of biologically plausible $S(x)$.

All simulations were carried out using the Chebfun library for MATLAB (T.A. Driscoll, N. Hale, L.N. Trefethen, 2014). Our spatial domain was consistently the periodic box *[-1, 1]*, with a discretization of 128 modes and a time step of $dt = 0.01$. Simulations were integrated to a final time $t_{end} = 30$. This value was determined numerically to be large relative to the timescale of relaxation to the steady state, and a sample of results were run to $2t_{end}$ and $4t_{end}$ to verify convergence. Initial conditions were generated as small random perturbations about the uniform steady state using Chebfun's randfun function, with spatial scale $\lambda = 0.1$. Upon convergence of each simulation, we defined a loss function estimating the relative quality of the final steady state. A weighting function ω was chosen as a measure of stripe location:

$$\omega(x) = \tanh\big(1000(|x| - 0.55)\big) - \tanh\big(1000(|x| - 0.75)\big) + \tanh\big(1000(|x| - 0.85)\big) \tanh\big(1000(|x| - 0.85)\big).$$

For a given simulation, this produced a 'coloring inside the lines' score via convolution against the final activator concentration:

$$L_1 = -\int_{-L}^{L} u_{C_i}(x)\omega(x)dx$$

Here, $u_{C_i}(x)$ is the final steady state observed subject to a modulator specified by amplitudes C_i.This functional value has the property that it decreases when u has high concentration in the expected stripe regions and increases when u is present between the desired peaks. Over the course of our investigation, we found that many potential prepatterns of varying complexity yielded good fits to the target. To this end, we added in a second component to the loss function as

$$L_2 = \frac{\epsilon_2 \sum_{i=1}^{12} |C_i| i}{\sqrt{\sum_{i=1}^{12} C_i^2}}$$

The weighting parameter ϵ_2 serves to modulate the degree to which higher spatial complexity of the prepattern is penalized. This value must be high enough so that simple patterns are optimal, but if too high the loss function will favor simple functions even if they yield subpar stripe patterns. After trial and error, we found the value of 0.1 was an effective middle ground, reliably yielding gradients which provided close fits to the target patterns. Finally, we included a third component of the loss function, L_3, which equals 10^{10} if u takes on negative, uniform, or exhibits NaN values and is zero otherwise. Collectively, then, we sought to find a coefficient set C_i which minimizes

$$L[C_i] \; = \; L_1[C_i] + \; L_2[C_i] + \; L_3[C_i] \, .$$

Taking advantage of the speed and accuracy of spectral methods, we approached this optimization problem by sampling ~40,000 sets of C_i per kinetic parameter by engaging MATLAB's implementation of the *patternsearch* algorithm, a widely used derivative-free optimization procedure. Starting from a set of random points in the function space, we identified the amplitudes C_i which established a Turing pattern that best matched the experimentally observed stripe pattern for each parameter discussed above. The gradient shown in Fig. 2E, along with the corresponding stripe pattern, is the optimized prepattern for the parameter μ.

3' -Single-cell RNA sequencing (scRNA-seq)

Sample preparation and library generation

Embryos from *R. pumilio and M. musculus* females were harvested at the relevant stages of pregnancy (i.e., E12.5-E15.5 for *M. musculus*; E13.5-E16.5 for *R. pumilio*). For all stages

(except *R. pumilio* E16.5, see below), a single, rectangular piece of dorsal skin, symmetrical across the midline, was micro-dissected, using the forelimbs and hindlimbs as reference points to maintain consistency across stages and species. For *R. pumilio* E16.5 embryos, regions R1 (dorsalmost, placode barren), R2 (dorsalmost, placode rich), and R3 (ventralmost, placode barren) were micro-dissected using morphological placodes as markers and regions from both sides of the midline were combined. Dorsal skins from 3 embryos were pooled (with the exception of *M. musculus* E13, N=2) into a single tube containing 1mL 0.25% Trypsin/PBS. Skins were minced with fine scissors and transferred to an Eppendorf tube containing 10 mL of 0.25% Trypsin/PBS. Tubes were incubated at 37°C in a hybridization oven with gentle rotation for 15-30 minutes (timing was dependent on embryonic stage) until the tissue was well dissociated. Primary cell suspensions were passed through a 70um filter and diluted 1:5 with 4% Bovine calf serum (BCS)/PBS. Cells were centrifuged at 300 x g in a refrigerated centrifuge set at 4°C for 10 minutes. Supernatant was discarded, the cell pellet was gently washed with 4% BCS/PBS and resuspended in 100 µl of 0.1% Ultrapure Bovine Serum Albumin (BSA)/PBS (Invitrogen). Cell number and viability was assessed using trypan exclusion and a TC20 automated cell counter (BioRad). Single cell RNA-sequencing libraries were generated using the Chromium Single Cell 3’ Reagent Kits (v2) (10x Genomics) following the manufacturer’s instructions. Libraries were sequenced on an Illumina NovaSeq 6000 (25 x 125bp, paired-end)

R. pumilio annotation

To generate gene annotations for the striped mouse genome suitable for analysis of bulk RNA-Seq data, we transferred high-quality NCBI gene annotations from the laboratory mouse (Mus_musculus.GRCm38.100.chr.gff3) to the *de novo R. pumilio* assembly. To accomplish this,

we used a homology-based lift-over procedure, implemented by the program LiftOff v1.4.1 using default parameters. Raw reads, genomes, and annotations have all been desposited under BioProject: PRJNA858857 BioSample: SAMN29758252.

Generation of a "Rhabdomyzed" genome

To both facilitate comparisons of transcriptomic data between *R. pumilio* and *M. musculus*, and to leverage the high quality gene annotations available for the latter, we generated an alternative, reference-guided assembly for the *R. pumilio* genome against which sequencing data was analyzed using previously described methods (Feigin et al., 2017). Briefly, genome reads for *R. pumilio* were aligned against the GRCm38 *M. musculus* genome using bwa-mem2 v2.1. Alignments were sorted and duplicates were removed with SortSam and MarkDuplicates from Picard tools (http://broadinstitute.github.io/picard/). Next, read pileups were generated using bcftools v1.11 (Li, 2011) programs mpileup, ignoring indels to preserve the reference GRCm38 coordinate system. Base calls were then generated using bcftools call's multiallelic caller. Finally, an initial reference-guided assembly was generated by projecting striped mouse base calls onto the reference mouse genome with bcftools consensus. This procedure was then repeated once more using the resulting consensus sequence from the first round as the new starting reference genome. Metrics using the *'Rhabdomyzed'* genome compared favorably (e.g., number of cells identified, median genes identified per cell, and percentage of genes confidently mapped to transcriptome) to a *R. pumilio* assembly/Liftover annotation and was thus chosen for downstream analyses.

Processing of raw single-cell RNA-seq data

Raw FASTQ reads from *R. pumilio* samples were mapped with Cell Ranger (version 3.1.0) to the *Rhabdomyzed Mus genome* (see above)*:* (Rhabdomys_to_Mus_bcftools_consensus3.fa/Mus_Musculus.GRCm38.101.gtf)

Raw FASTQ reads from *M. musculus* samples were mapped with Cell Ranger (version 3.1.0) to the *M. musculus* mm10 reference genome (GRCm38.94.dna/GRCm38.84.gtf).

Doublet/multiplet simulation and low-quality cell filtering

Raw count matrices from *R. pumilio* and *M. musculus* obtained from alignment with the *'Rhabdomyzed' Mus* genome *or* mm10 reference genome, respectively, were pre-processed and doublet/multiplets were simulated using Single-Cell Remover of Doublets (Scrublet) (Wolock et al., 2019) (version 0.2.1) with default parameters enabled. The doublet/multiplet score threshold was adjusted manually to intersect the bimodal distribution of the observed transcriptomes on the probability density histogram as suggested. Putative singlets were kept and used for downstream query and comparative analyses if and only if they met the following user-defined collective quality control metrics filtering criteria: a) cells with more than 350 but less than 5,000 genes were kept; b) cells containing less than 10% total mitochondrial gene content were kept; c) cells not identified as outliers falling outside a prediction confidence interval defined by a quadratic in a model of a gene vs. counts plot (P-value $1e^{-3}$) were kept (Fan et al., 2016).

Anchoring, integration, and downstream analysis of single-cell RNA-seq data

We performed anchoring and integration of *R. pumilio* or *M. musculus* data sets using the Seurat package (Version 3.2.2, R Studio version 3.6.1) (Stuart et al., 2019). In brief, species-specific

Seurat objects were created using individual, raw digitized count matrices as suggested by developer. Objects were merged and individual gene expression matrices were normalized, and variable genes/features identified. Data sets were anchored (n=30 dimensions) and integrated (n=30 dimensions). The integrated object was then scaled. Significant PCs used for clustering and neighbor-finding were identified using a combination of statistical and heuristic methods. Neighbors and clusters were identified with dimensions specified by user and visualized using two-dimensional t-distributed Stochastic Neighbor Embedding (tSNE) embedding. For all analysis, R1, R2, and R3 from *R. pumilio* E16.5 embryos were randomly down sampled to equal cell numbers before integration into a single object that was representative of E16.5 *R. pumilio* dorsal skin.

Cell type annotation

Cell types in *R. pumilio* and *M. musculus* were defined and annotated using a core set of *bona fide* E14.5 *M. musculus* gene biomarkers (Sennett et al., 2015) and are reported in Table S2. Aggregate biomarker gene module scores were computed in Seurat. Aggregate biomarker gene module scores and individual gene expression profiles were Log-normalized and visualized as feature plots in two-dimensional tSNE embedding.

Quantification of Sfrp2^{+} fibroblasts

To quantify the number of *Sfrp2*$^{+}$ fibroblasts in *R. pumilio* and *M. musculus*, we randomly sub-sampled *Sfrp2*$^{+}$ fibroblasts ($Sfrp2_{\text{normalized counts}} > 0$) in *R. pumilio* or *M. musculus* (n=25 iterations). To mitigate potential differences owed to sample size, we sub-sampled fibroblasts to the lowest number of total fibroblasts in anyone comparison. *Sfrp2*$^{+}$ fibroblasts in *R. pumilio* or

M. musculus were then normalized to total fibroblasts. Results from each iteration are plotted with confidence intervals and their correlation was determined with Spearman's correlation. Results are represented as the average ratio of *Sfrp2*$^{+}$ fibroblasts to total fibroblasts from 25 different iterations ± STDV.

Gene expression analysis

To quantify gene expression changes in *R. pumilio* fibroblasts that correlate with *Sfrp2* expression levels, we performed three sub-samplings of fibroblasts based on *Sfrp2* UMI counts: (1.) *Sfrp2*-high > 1.0; *Sfrp2*-low < 1, (2.) *Sfrp2*-high > 2; *Sfrp2*-low < 2, and (3.) *Sfrp2*-high > 3; *Sfrp2*-low < 3. Gene expression analysis was performed in Seurat (Wilcoxon Rank Sum test) to identify differentially expressed genes (DEGs, adjusted p-value < 0.05). Although good agreement was observed in all sub-samplings used, only genes identified as differential in all three sub-sampling were subjected to Gene Ontology analysis using Enrichr and significant GOs (P_{adj} <0.05) were considered.

Latent time and RNA dynamics analysis

Putative fibroblasts from all developmental stages from *R. pumilio* or *M. musculus* were sub-clustered and used to compute a two-dimensional Force Layout Embedding with Pegasus (version 1.3.0). Loom files were created using the Python script *velocyto.py* (version 0.17.17; Anaconda version 2020.07) for each individual *R. pumilio* and *M. musculus* library/developmental stage. Loom files were combined using loompy (version 2.0.16; Anaconda version 3.6-5.0.1; Python version 3.7.2; Spyder version 4.1.5). We computed individual region-specific terminal states (i.e., R1, R2, or R3 in E15.5) from initial state E12.5 and estimated their

fate probabilities toward them using CellRank (version 0.2.2; Python version 3.7.0) (Lange et al., 2022). Gene trends were calculated along distinct lineages in the identified terminal states in latent time (set manually to 1.0).

***In situ* hybridization chain reaction (HCR)**

A conserved region in the *Sfrp2* mRNA between *R. pumilio* and *M. musculus* was used to generate 16 probe binding sequences for *in situ* hybridization chain reaction (HCR). HCR was performed using the standard protocol for fixed frozen tissue sections available from Molecular Instruments®. High signal within limb sections of both species was used as a positive control.

Immunofluorescence

Immuno-fluorescence was performed on tissue sections using standard procedures. Briefly, slides were washed with 1x PBS with 0.1% Tween (PBT) and blocked with 1x PBT/3% Bovine serum albumin (BSA) for 1 hour. Primary antibodies rabbit anti-LEF1 (Cell signaling #2230S, 1:100), rabbit anti-β-catenin (Sigma # C2206, 1:500), chicken anti-GFP (Novus Biologicals # NB100-1614, 1:200), or rabbit anti-Krt14 (BioLegend #905301, 1:1000) were diluted in 1x PBT/3%BSA and slides were incubated at 4°C O/N. The next morning, slides were washed several times with 1x PBT and secondary antibodies (goat anti-mouse Alexa Fluor 488, ThermoFisher, #A-21133) or (goat anti-mouse Alexa Fluor 546, ThermoFisher, #A-11001) were diluted 1:500 in 1x PBT/3%BSA and slides were incubated for 1 hour at room temperature. Slides were washed several times with 1x PBT, stained with DAPI to visualize nuclei, and mounted for imaging. Images were taken on a Nikon A1R confocal microscope. At least 3 embryos per condition were analyzed.

Generation of *Rosa*$^{Sfrp2\text{-}GFP}$ laboratory mice

Srfp2 cDNA was synthesized (Azenta) and cloned into pR26 CAG/T2AGFP Asc (pR26 CAG/GFP Asc was a gift from Ralf Kuehn, Addgene plasmid # 74285, and modified to contain a T2A instead of IRES). The plasmid was inserted into the *Rosa26* locus by CRISPR-Cas9-mediated gene targeting. Cas9 (IDT) was complexed with an sgRNA (Millipore-Sigma) having the spacer sequence 5'- ACTCCAGTCTTTCTAGAAGA-3'. C57BL/6J zygotes were microinjected and transferred into pseudopregnant recipients. Founders were screened for the presence of GFP by PCR using primers GFP(F) and GFP(R)12 founders were further screened for 5' end targeting using primers ROSA26J and SAR and for 3' end targeting using GFP(F) and ROSA26L. All 12 were correctly targeted, 10 were chosen to confirm the presence of the cDNA by Sanger sequencing. Primer sequences are available in Table S4.

Quantification of hair follicle number

To examine the effect of dermal *Sfrp2* over-expression on hair follicle number, *Rosa*$^{Sfrp2\text{-}GFP}$ females were crossed to *Dermo1-Cre* (JAX stock #008712) (Šošić et al., 2003; Yu et al., 2003) males and embryos were collected at E17.5. Embryos were fixed, embedded, and immunostained for GFP, as described above. GFP expression was mosaic, but a posterior dorsal region consistently showed high levels of GFP signal across all GFP (+) embryos. Within this region, follicle quantification was performed on equally sized areas of the skin after performing hematoxylin-eosin (H&E) stains to reliably identify hair follicles. In total, 4 double-transgenic and 4 control embryos were quantified. For each embryo, hair follicle number from 4 skin sections were counted and averaged with an equal sized region of the embryo. Statistical

significance was assessed using an unpaired t-test. Statistical significance was assigned to p-values: $p<0.05$(*); $p<0.01$(**), $p<0.001$(***), $p<0.0001$(****).

Quantitative Real Time PCR (qPCR)

Individual dorsal skin regions R1-R3 were dissected using either hair placodes (E16.5), hair length (E19.5) or pigmentation (P0, P4) as markers. Skin sections were stored in 500ul of RNALater (Invitrogen) and kept at -20°C until RNA extraction. RNA was extracted using the RNeasy fibrous tissue mini kit (QIAGEN) per the manufacturer's protocol. cDNA synthesis was carried out using qScript cDNA SuperMix (Quantabio) and qPCR for *Sfrp2* was performed using SYBR Green qPCR Reagent (Quantabio) on a ViiA 7 Real-Time PCR machine (Applied Biosystems). Primers used for qPCR are listed in Table S4.

Over-expression of *Sfrp2* in melanocytes

The LV-*GFP* plasmid used in this study has been described previously(Beronja et al., 2010). To generate LV-*SFRP2-GFP*, we amplified the *Sfrp2* coding sequence from an *Sfrp2* (NM_009144) Mouse Tagged ORF Clone (Origene CAT#: MR204070) using CloneAmp™ HiFi PCR Premix (Takara 639298) and cloned it (in frame) into the linearized LV-*GFP* plasmid using In-Fusion® Snap Assembly Master Mix (Takara #638947). High titer viruses were generated as previously described (Beronja et al., 2010). Prior to transfection, MelanA cells (purchased from the Wellcome Trust Functional Genomics Cell Bank at St. George's, University of London) were seeded in RPMI 1640 media supplemented with penicillin (100,000 U/L), streptomycin (100 mg/L), fetal bovine serum (10%), and tetradecanoyl phorbol acetate (TPA) (200nM). At ~80% confluency, cells were centrifuged for 30min at 37ºC and media was aspirated away and

replenished with fresh media lacking antibiotics. LV-*GFP* or LV-*SFRP2-GFP* viral supernatant was added to each well along with a 1mg/mL polybrene diluted in bovine calf serum. Plates were gently swirled and incubated at 37°C/5% CO_2 for 30 minutes. Plates were then centrifuged at 1100 x g for 30 minutes at 37°C. Media was removed, cells were rinsed twice with PBS, and fresh media was added. To enrich for cells with high transfection efficiency, cells with high GFP expression were sorted by fluorescence activated cell sorting (FACS) on a BD FACSAria II (BD Biosciences), grown to confluency, sorted one additional time, and grown to ~80% confluency. Media was removed, cells were incubated in 500ul TriReagent (Zymo) for 5 minutes, flash frozen in liquid nitrogen, and stored at -80°C. RNA was isolated using a direct-zol RNA microprep kit (Zymo). cDNA synthesis was carried out using qScript cDNA SuperMix (Quantabio) and qPCR for *Mitf*, *Tyr*, *Axin2*, *C-myc*, and *Ccnd1* was performed using SYBR Green qPCR Reagent (Quantabio) on a ViiA 7 Real-Time PCR machine (Applied Biosystems), as described above. Primers used for qPCR are listed in Table S4.

In vivo genome editing in _R. pumilio_

Generation of immortalized R. pumilio fibroblasts

A skin biopsy was obtained from the flank of an adult male *R. pumilio* dermal fibroblasts were subsequently isolated following a previously published protocol(Aasen and Izpisúa Belmonte, 2010). In brief, hair, fat, and connective tissue were scraped away from the biopsy before digesting O/N at 4°C in HBSS without Ca^{2+} and Mg^{2+} (Thermo Fisher) containing dispase at a final concentration of 500 caseinolytic units/mL (Corning) and an antibiotic/antimycotic solution final concentrations of 100 µg/mL streptomycin, 100 IU/mL penicillin, and 250 ng/mL amphotericin B (HyClone). Following digestions, the epidermis was removed and discarded. The

865 dermis was cut into small pieces, moistened with Dulbecco's modified Eagle medium (Thermo
866 Fisher; DMEM), and pressed into grooves scored into the wells of a 6-well tissue culture dish.
867 The dermis was maintained in DMEM containing 10% (vol/vol) fetal bovine serum (Omega
868 Scientific) and 1% (vol/vol) penicillin/streptomycin (Corning) at 37°C, 5% (vol/vol) CO_2. Media
869 was changed every 4–5 days and cultures monitored for fibroblast growth. Once sufficient
870 outgrowth had occurred, the dermis was removed from the plate and the fibroblasts removed by
871 trypsinization (0.05% trypsin-EDTA; Gibco) for expansion into larger culture dishes.
872
873 To generate the immortalized dermal fibroblast cell line, γ-retroviral pseudoparticles containing a
874 transfer plasmid encoding simian virus 40 (SV40) large T antigen (Hahn et al., 2002) were
875 produced in HEK293T cells. Cells were cultured on poly-L-lysine–coated 10 cm plates at 37°C,
876 5% (vol/vol) CO_2 in 10% FBS DMEM. At ~80% confluency, Xtremegene HP DNA transfection
877 reagent (Roche Applied Science) was utilized per manufacturer's directions to co-transfect the
878 cells with 4 µg pBABE-neo-SV40 large T, a generous gift from Bob Weinberg (Addgene
879 plasmid #1780; http://n2t.net/addgene:1780; RRID:Addgene_1780); 4 µg of a plasmid
880 containing the genes for Moloney murine leukemia virus gag-pol; and 0.57 µg of a plasmid
881 containing the gene for the G envelope protein of vesicular stomatitis virus. Supernatants were
882 harvested 24, 48, and 72 hr post-transfection, stored at 4°C, and then pooled before passing
883 through a 0.45 µm membrane filter (Millipore). Polybrene (Sigma-Aldrich; final concentration, 4
884 µg/mL) and HEPES (Gibco; final concentration, 2 mM) were added to the filtered supernatants;
885 aliquots were prepared and at −80°C until needed. Primary dermal fibroblasts were seeded in 6-
886 well plates for transduction so that cell confluency was 30–40% at the time of transduction. The
887 cells were "spinoculated" in a centrifuge at 37°C, 931 rcf for 2 h with 2 mL of thawed, undiluted

γ-retroviral pseudoparticles per well. The cells were subsequently kept at 37°C, 5% (vol/vol) CO_2 and the media replaced with 10% FBS DMEM 6 hours post-spinoculation. The transduced cells were pooled once they achieved ~80% confluency in the 6-well plate and subsequently expanded to prepare immortalized cell stocks. Cells were verified as negative for mycoplasma by testing with the MycoAlert Mycoplasma Detection Assay kit (Lonza) per the manufacturer's instructions.

Guide-RNA design and testing

We designed 9 CRISPR sgRNAs targeting the *R. pumilio Sfrp2* exon1 using CRISPOR (Concordet and Haeussler, 2018). We then cloned each guide into the rAAV Nme2*Cas9* plasmid (Edraki et al., 2019) by replacing sg*Tyr* with sg*Sfrp2* (Yoon et al., 2018). Next, we transfected each AAV.Nme2*Cas9*.sg*Sfrp2* into immortalized striped mouse immortalized fibroblasts using lipofectamine3000 (L300008, Thermo Fisher). ~3-4 days post transfection, we extracted genomic DNA using the Zymo Quick DNA Miniprep Plus Kit (Zymo) and performed targeted PCR on *Sfrp2* (primers are listed in Table S4). We then performed a T7E1 nuclease assay (M0302, New England Biolabs) according to the manufacturer's protocol and resolved digested products on a 1.2% agarose gel containing STBY™ safe DNA gel stain (Invitrogen) to assess excision efficiency of each designed sgRNA.

rAAV production, in vivo transduction, and genotyping

rAAV6. Nme_2*Cas9*.sg*Sfrp2* was produced, concentrated, and purified by the PNI viral core facility at Princeton University. Female *R. pumilio* between 4 and 6 months of age were chosen to breed with age matched males. The presence of vaginal mating plugs or sperm was designated

as days post coitum (d.p.c) 0.5. Pregnant females at d.p.c. 0.75 (N = 21) were anesthetized, administered with analgesics, and aseptically prepared for survival surgery. To deliver rAAV, we slowly injected 0.5-1 μL rAAV (about 1~3×10^9 genome copy (GC)) mixed with Chicago Sky Blue dye (0.1%, Fisher Scientific, Cat # AAA1424214) into the oviduct ampulla using a glass micropipette with tip diameter of ~10-30 μm. The injection technique in *R. pumilio* was optimized based on previously described procedures in *M. musculus* (Sato, 2005; Yoon et al., 2018). Operated animals were allowed to carry to term and pups were genotyped as follows: We collected ear punch tissue from individual animals and extracted genomic DNA using a Zymo Quick DNA Miniprep Plus Kit (Zymo). Next, we PCR amplified the genomic region containing the guide targeting site (primers are listed on Table S4) and resolved PCR amplicons using agarose gel electrophoresis. For F0 striped mice, PCR amplicons were further cloned into a pSC-amp/kan vector using StrataClone PCR cloning kit (240205, Agilent Technologies). We picked ~20-50 single colonies per sample to determine the presence, composition, and frequency of targeted mutations via Sanger sequencing.

For knocking out *Tyr* in *R. pumilio*, 29 females were injected, 43 pups were obtained, and 9 of them carried gene edits in *Tyr*. Of these, we obtained one albino pup of homozygous knockout (*Tyr*$^{-/-}$) (Fig.6B). 6 F0 founders were mated to wild-type animals to obtain germline transmission. Of these 6 founders, all of them successfully produced heterozygous animals.

For knocking out *Sfrp2* in *R. pumilio*, 21 females were injected, 57 pups were obtained, and 14 of them carried gene edits in *Sfrp2*. Of these, 11 F0 founders were mated to wild-type animals to obtain germline transmission. We obtained a total of 4 mutated alleles (2bp deletion, 13bp deletion, 466bp deletion, and 527 bp deletion); all of which produce a frameshift. 10 out of 11

founders tested successfully produced heterozygous F1 animals. F1 heterozygous striped mice containing the same mutated alleles were crossed to produce F2 animals. Genotypes of all F2 animals, determined by a combination of PCR, TOPO cloning, and Sanger sequencing, showed a mendelian ratio distribution (WT: N = 30; Heterozygous: N = 65; Homozygous: N = 27). At least two independently generated null alleles were tested in phenotypic analyses. Our designation of *Sfrp2*$^{-/-}$ mice encompasses animals that either share the same mutated allele or have a combination of two different mutated alleles.

Western blots

We collected fresh liver tissues of euthanized animals and prepared protein lysates in RIPA (50 mM Tris-HCl pH 8.0, 150 mM NaCl, 0.1%SDS, 0.5% Sodium deoxycholate, 0.1% Triton-X, 1 mM EDTA) supplemented with protease inhibitor cocktail (ab271306, Abcam). Protein concentration was quantified by Pierce Detergent Compatible Bradford Assay (Thermal Scientific). For SDS-PAGE, we loaded 20 μg of total protein per sample. Membranes were probed with primary antibodies at 4℃ O/N, washed with TBST 4x, and incubated in secondary antibody for 1 hour at room temperature. Primary antibodies: 1:100 *Sfrp2* (ab137560, Abcam, Cambridge, UK), 1:1000 β-tubulin (mAb #86298, Cell Signaling). Secondary antibodies: 1:20000 IRDye® 800CW Goat anti-Rabbit IgG (926-32211, LI-COR Biosciences), 1:20000 IRDye 680RD Goat anti-Mouse IgG system (926-68070, LI-COR Biosciences). Membranes were developed using an Odyssey CLx imaging system (LI-COR Biosciences).

Quantification of *Sfrp2*$^{-/-}$ phenotypes

Stripe width: Dorsal skin from equally staged P3 striped mouse *Sfrp2*$^{-/-}$ (N=7) or *Sfrp2*$^{+/+}$ (N=10) pups was dissected and flat-mount skins were prepped. Images of pinned skins were taken within a uniform lighting box with an EIOS2000D camera (Canon) at equal magnification. To quantify stripe width, FIJI (ImageJ) was used to draw line segments spanning each region of interest. For each image, 10 horizontal lines were measured along the Anterior posterior axis of the skin and an average width was calculated. For R1, R2, and R3, this was performed on each side of the midline. To measure width of the "striped area", 10 lines were drawn connecting the most ventral boundary of R3 on both sides and averaged. "Width (% of striped area)" was calculated by dividing the average width of each region (i.e., R1, R2, R3, and midline) by the average width of the stripe area. Statistical significance was assessed using unpaired t-tests. Statistical significance was assigned to p-values: $p<0.05$(*); $p<0.01$(**), $p<0.001$(***), $p<0.0001$(****).

Pigmentation: A single image of 6 *R. pumilio* adults (3 *Sfrp2*$^{+/+}$, 3 *Sfrp2*$^{-/-}$) was taken within a uniform lighting box with an EIOS2000D camera (Canon). To ensure image was true to color, color correction was performed on the image using a Pixel Perfect color checker and Adobe Lightroom software. To quantify pigment differences across animals, a consistently sized region of interest (ROI) was drawn within each stripe region and mean gray value within the ROI was measured using Adobe Photoshop. For R1-R3, mean gray values were measured in 3 subregions within each stripe region, on each side of the midline (6 ROIs total) and averaged. For the midline, mean gray values were measured in 5 subregions within the midline and averaged. Statistical significance was assessed using unpaired t-tests. Statistical significance was assigned to p-values: $p<0.05$(*); $p<0.01$(**), $p<0.001$(***), $p<0.0001$(****).

Excel Tables

Table S1: Differentially expressed genes between Region 1-4 of E16.5 striped mice skin.

(Table_S1.xls)

Table S3: Differentially expressed genes between Sfrp2^{high} and Sfrp2^{low} fibroblast populations.

(Table_S3.xls)

Multimedia Files

Supplemental Movie 1: Changes in regulator distribution alter the simulated stripe pattern.

(Supplemental_Movie_1.mp4)

References

Aasen, T., and Izpisúa Belmonte, J.C. (2010). Isolation and cultivation of human keratinocytes from skin or plucked hair for the generation of induced pluripotent stem cells. Nat. Protoc. *5*, 371–382.

Andl, T., Reddy, S.T., Gaddapara, T., and Millar, S.E. (2002). WNT signals are required for the initiation of hair follicle development. Dev. Cell *2*, 643–653.

Bailleul, R., Curantz, C., Desmarquet-Trin Dinh, C., Hidalgo, M., Touboul, J., and Manceau, M. (2019). Symmetry breaking in the embryonic skin triggers directional and sequential plumage patterning. PLoS Biol. *17*, e3000448.

Beronja, S., Livshits, G., Williams, S., and Fuchs, E. (2010). Rapid functional dissection of genetic networks via tissue-specific transduction and RNAi in mouse embryos. Nat. Med. *16*, 821–827.

Caro, T. (2005). The Adaptive Significance of Coloration in Mammals. Bioscience *55*, 125–136.

Caro, T., and Mallarino, R. (2020). Coloration in Mammals. Trends Ecol. Evol. *35*, 357–366.

Concordet, J.-P., and Haeussler, M. (2018). CRISPOR: intuitive guide selection for CRISPR/Cas9 genome editing experiments and screens. Nucleic Acids Res. *46*, W242–W245.

Conway, J.R., Lex, A., and Gehlenborg, N. (2017). UpSetR: an R package for the visualization of intersecting sets and their properties. Bioinformatics *33*, 2938–2940.

Edraki, A., Mir, A., Ibraheim, R., Gainetdinov, I., Yoon, Y., Song, C.-Q., Cao, Y., Gallant, J., Xue, W., Rivera-Pérez, J.A., et al. (2019). A Compact, High-Accuracy Cas9 with a Dinucleotide PAM for In Vivo Genome Editing. Mol. Cell *73*, 714-726.e4.

Eizirik, E., David, V.A., Buckley-Beason, V., Roelke, M.E., Schäffer, A.A., Hannah, S.S., Narfström, K., O'Brien, S.J., and Menotti-Raymond, M. (2010). Defining and Mapping Mammalian Coat Pattern Genes: Multiple Genomic Regions Implicated in Domestic Cat Stripes and Spots. Genetics *184*, 267–275.

Enshell-Seijffers, D., Lindon, C., Wu, E., Taketo, M.M., and Morgan, B.A. (2010). β-Catenin activity in the dermal papilla of the hair follicle regulates pigment-type switching. Proceedings of the National Academy of Sciences *107*, 21564–21569.

Fan, J., Salathia, N., Liu, R., Kaeser, G.E., Yung, Y.C., Herman, J.L., Kaper, F., Fan, J.-B., Zhang, K., Chun, J., et al. (2016). Characterizing transcriptional heterogeneity through pathway and gene set overdispersion analysis. Nat. Methods *13*, 241–244.

Feigin, C.Y., Newton, A.H., Doronina, L., Schmitz, J., Hipsley, C.A., Mitchell, K.J., Gower, G., Llamas, B., Soubrier, J., Heider, T.N., et al. (2017). Genome of the Tasmanian tiger provides insights into the evolution and demography of an extinct marsupial carnivore. Nature Ecology & Evolution *2*, 182–192.

Fuchs, E. (2007). Scratching the surface of skin development. Nature *445*, 834–842.

Fuchs, E., and Raghavan, S. (2002). Getting under the skin of epidermal morphogenesis. Nat. Rev. Genet. *3*, 199–209.

Gat, U., DasGupta, R., Degenstein, L., and Fuchs, E. (1998). De Novo hair follicle morphogenesis and hair tumors in mice expressing a truncated beta-catenin in skin. Cell *95*, 605–614.

Gierer, A., and Meinhardt, H. (1972). A theory of biological pattern formation. Kybernetik *12*, 30–39.

Gupta, K., Levinsohn, J., Linderman, G., Chen, D., Sun, T.Y., Dong, D., Taketo, M.M., Bosenberg, M., Kluger, Y., Choate, K., et al. (2019). Single-Cell Analysis Reveals a Hair Follicle Dermal Niche Molecular Differentiation Trajectory that Begins Prior to Morphogenesis. Dev. Cell *48*, 17-31.e6.

Hahn, W.C., Dessain, S.K., Brooks, M.W., King, J.E., Elenbaas, B., Sabatini, D.M., DeCaprio, J.A., and Weinberg, R.A. (2002). Enumeration of the simian virus 40 early region elements necessary for human cell transformation. Mol. Cell. Biol. *22*, 2111–2123.

Hardy, M.H. (1992). The secret life of the hair follicle. Trends Genet. *8*, 55–61.

Haupaix, N., and Manceau, M. (2020). The embryonic origin of periodic color patterns. Dev. Biol. *460*, 70–76.

Haupaix, N., Curantz, C., Bailleul, R., Beck, S., Robic, A., and Manceau, M. (2018). The periodic coloration in birds forms through a prepattern of somite origin. Science *361*. https://doi.org/10.1126/science.aar4777.

He, T.C., Sparks, A.B., Rago, C., Hermeking, H., Zawel, L., da Costa, L.T., Morin, P.J., Vogelstein, B., and Kinzler, K.W. (1998). Identification of c-MYC as a target of the APC pathway. Science *281*, 1509–1512.

Hiscock, T.W., and Megason, S.G. (2015). Orientation of Turing-like Patterns by Morphogen Gradients and Tissue Anisotropies. Cell Syst *1*, 408–416.

Iozumi, K., Hoganson, G.E., Pennella, R., Everett, M.A., and Fuller, B.B. (1993). Role of tyrosinase as the determinant of pigmentation in cultured human melanocytes. J. Invest. Dermatol. *100*, 806–811.

Jho, E.-H., Zhang, T., Domon, C., Joo, C.-K., Freund, J.-N., and Costantini, F. (2002). Wnt/beta-catenin/Tcf signaling induces the transcription of Axin2, a negative regulator of the signaling pathway. Mol. Cell. Biol. *22*, 1172–1183.

Johansson, J.A., and Headon, D.J. (2014). Regionalisation of the skin. Semin. Cell Dev. Biol. *25–26*, 3–10.
Johnson, M.R., Barsh, G.S., and Mallarino, R. (2019). Periodic patterns in Rodentia: Development and evolution. Exp. Dermatol. *28*, 509–513.
Kaelin, C.B., and Barsh, G.S. (2013). Genetics of pigmentation in dogs and cats. Annu Rev Anim Biosci *1*, 125–156.
Kaelin, C.B., Xu, X., Hong, L.Z., David, V.A., McGowan, K.A., Schmidt-Küntzel, A., Roelke, M.E., Pino, J., Pontius, J., Cooper, G.M., et al. (2012). Specifying and sustaining pigmentation patterns in domestic and wild cats. Science *337*, 1536–1541.
Kaelin, C.B., McGowan, K.A., and Barsh, G.S. (2021). Developmental genetics of color pattern establishment in cats. Nat. Commun. *12*, 5127.
Kaufman, M.H. (1992). The Atlas of Mouse Development (London, England: Academic Press Limited).
Keller, S.H., Jena, S.G., Yamazaki, Y., and Lim, B. (2020). Regulation of spatiotemporal limits of developmental gene expression via enhancer grammar. Proceedings of the National Academy of Sciences *117*, 15096–15103.
Kim, M., Han, J.H., Kim, J.-H., Park, T.J., and Kang, H.Y. (2016). Secreted Frizzled-Related Protein 2 (sFRP2) Functions as a Melanogenic Stimulator; the Role of sFRP2 in UV-Induced Hyperpigmentary Disorders. J. Invest. Dermatol. *136*, 236–244.
Kondo, S. (2017). An updated kernel-based Turing model for studying the mechanisms of biological pattern formation. J. Theor. Biol. *414*, 120–127.
Kondo, S., and Miura, T. (2010). Reaction-Diffusion Model as a Framework for Understanding Biological Pattern Formation. Science *329*, 1616–1620.
Kuriyama, T., and Hasegawa, M. (2017). Embryonic developmental process governing the conspicuousness of body stripes and blue tail coloration in the lizardPlestiodon latiscutatus. Evol. Dev. *19*, 29–39.
Lange, M., Bergen, V., Klein, M., Setty, M., Reuter, B., Bakhti, M., Lickert, H., Ansari, M., Schniering, J., Schiller, H.B., et al. (2022). CellRank for directed single-cell fate mapping. Nat. Methods *19*, 159–170.
Li, H. (2011). A statistical framework for SNP calling, mutation discovery, association mapping and population genetical parameter estimation from sequencing data. Bioinformatics *27*, 2987–2993.
Liang, C.-J., Wang, Z.-W., Chang, Y.-W., Lee, K.-C., Lin, W.-H., and Lee, J.-L. (2019). SFRPs Are Biphasic Modulators of Wnt-Signaling-Elicited Cancer Stem Cell Properties beyond Extracellular Control. Cell Rep. *28*, 1511-1525.e5.
Lin, H., Angeli, M., Chung, K.J., Ejimadu, C., Rosa, A.R., and Lee, T. (2016). sFRP2 activates Wnt/β-catenin signaling in cardiac fibroblasts: differential roles in cell growth, energy metabolism, and extracellular matrix remodeling. Am. J. Physiol. Cell Physiol. *311*, C710–C719.
van Loon, K., Huijbers, E.J.M., and Griffioen, A.W. (2021). Secreted frizzled-related protein 2: a key player in noncanonical Wnt signaling and tumor angiogenesis. Cancer Metastasis Rev. *40*, 191–203.
Mallarino, R., Henegar, C., Mirasierra, M., Manceau, M., Schradin, C., Vallejo, M., Beronja, S., Barsh, G.S., and Hoekstra, H.E. (2016). Developmental mechanisms of stripe patterns in rodents. Nature *539*, 518–523.
Mallarino, R., Pillay, N., Hoekstra, H.E., and Schradin, C. (2018). African striped mice. Curr. Biol. *28*, R299–R301.

Michael I Love, Wolfgang Huber, Simon Anders (2014). Moderated estimation of fold change and dispersion for RNA-seq data with DESeq2. Genome Biology.

Millar, S.E. (2002). Molecular mechanisms regulating hair follicle development. J. Invest. Dermatol. *118*, 216–225.

Mills, M.G., and Patterson, L.B. (2009). Not just black and white: pigment pattern development and evolution in vertebrates. Semin. Cell Dev. Biol. *20*, 72–81.

Morgan, B.A. (2014). The dermal papilla: an instructive niche for epithelial stem and progenitor cells in development and regeneration of the hair follicle. Cold Spring Harb. Perspect. Med. *4*, a015180.

Murakami, A., Hasegawa, M., and Kuriyama, T. (2018). Developmental mechanisms of longitudinal stripes in the Japanese four-lined snake. J. Morphol. *279*, 27–36.

Parichy, D.M. (2003). Pigment patterns: fish in stripes and spots. Curr. Biol. *13*, R947-50.

Patterson, L.B., and Parichy, D.M. (2019). Zebrafish Pigment Pattern Formation: Insights into the Development and Evolution of Adult Form. Annu. Rev. Genet. *53*, 505–530.

Rezza, A., Wang, Z., Sennett, R., Qiao, W., Wang, D., Heitman, N., Mok, K.W., Clavel, C., Yi, R., Zandstra, P., et al. (2016). Signaling Networks among Stem Cell Precursors, Transit-Amplifying Progenitors, and their Niche in Developing Hair Follicles. Cell Rep. *14*, 3001–3018.

Sato, M. (2005). Intraoviductal introduction of plasmid DNA and subsequent electroporation for efficient in vivo gene transfer to murine oviductal epithelium. Mol. Reprod. Dev. *71*, 321–330.

Sennett, R., Wang, Z., Rezza, A., Grisanti, L., Roitershtein, N., Sicchio, C., Mok, K.W., Heitman, N.J., Clavel, C., Ma'ayan, A., et al. (2015). An Integrated Transcriptome Atlas of Embryonic Hair Follicle Progenitors, Their Niche, and the Developing Skin. Dev. Cell *34*, 577–591.

Shtutman, M., Zhurinsky, J., Simcha, I., Albanese, C., D'Amico, M., Pestell, R., and Ben-Ze'ev, A. (1999). The cyclin D1 gene is a target of the beta-catenin/LEF-1 pathway. Proc. Natl. Acad. Sci. U. S. A. *96*, 5522–5527.

Sick, S., Reinker, S., Timmer, J., and Schlake, T. (2006). WNT and DKK determine hair follicle spacing through a reaction-diffusion mechanism. Science *314*, 1447–1450.

Song, Y., Yang, R., and Sun, G. (2017). Pattern dynamics in a Gierer–Meinhardt model with a saturating term. Appl. Math. Model. *46*, 476–491.

Song, Y., Boncompagni, A.C., Kim, S.-S., Gochnauer, H.R., Zhang, Y., Loots, G.G., Wu, D., Li, Y., Xu, M., and Millar, S.E. (2018). Regional Control of Hairless versus Hair-Bearing Skin by Dkk2. Cell Rep. *25*, 2981-2991.e3.

Šošić, D., Richardson, J.A., Yu, K., Ornitz, D.M., and Olson, E.N. (2003). Twist Regulates Cytokine Gene Expression through a Negative Feedback Loop that Represses NF-κB Activity. Cell *112*, 169–180.

Steingrímsson, E., Copeland, N.G., and Jenkins, N.A. (2004). Melanocytes and the microphthalmia transcription factor network. Annu. Rev. Genet. *38*, 365–411.

Stuart, T., Butler, A., Hoffman, P., Hafemeister, C., Papalexi, E., Mauck, W.M., 3rd, Hao, Y., Stoeckius, M., Smibert, P., and Satija, R. (2019). Comprehensive Integration of Single-Cell Data. Cell *177*, 1888-1902.e21.

T.A. Driscoll, N. Hale, L.N. Trefethen (2014). Chebfun Guide (Oxford: Pafnuty Publications).

Tsai, S.-Y., Sennett, R., Rezza, A., Clavel, C., Grisanti, L., Zemla, R., Najam, S., and Rendl, M. (2014). Wnt/β-catenin signaling in dermal condensates is required for hair follicle formation. Dev. Biol. *385*, 179–188.

Turing, A.M. (1990). The chemical basis of morphogenesis. 1953. Bull. Math. Biol. *52*, 153–197; discussion 119-52.

Van Gorder, R.A. (2021). Pattern formation from spatially heterogeneous reaction-diffusion systems. Philos. Trans. A Math. Phys. Eng. Sci. *379*, 20210001.

Vittadello, S.T., Leyshon, T., Schnoerr, D., and Stumpf, M.P.H. (2021). Turing pattern design principles and their robustness. Philosophical Transactions of the Royal Society A: Mathematical, Physical and Engineering Sciences *379*, 20200272.

Wei, J., and Winter, M. (2014). The Gierer-Meinhardt System with Saturation. In Mathematical Aspects of Pattern Formation in Biological Systems, J. Wei, and M. Winter, eds. (London: Springer London), pp. 249–261.

Wolock, S.L., Lopez, R., and Klein, A.M. (2019). Scrublet: Computational Identification of Cell Doublets in Single-Cell Transcriptomic Data. Cell Syst *8*, 281-291.e9.

Wu, J., and Wang, X. (2019). Whole-Mount In Situ Hybridization of Mouse Embryos Using DIG-Labeled RNA Probes. Methods Mol. Biol. *1922*, 151–159.

Yoon, Y., Wang, D., Tai, P.W.L., Riley, J., Gao, G., and Rivera-Pérez, J.A. (2018). Streamlined ex vivo and in vivo genome editing in mouse embryos using recombinant adeno-associated viruses. Nat. Commun. *9*, 1–12.

Yu, K., Xu, J., Liu, Z., Sosic, D., Shao, J., Olson, E.N., Towler, D.A., and Ornitz, D.M. (2003). Conditional inactivation of FGF receptor 2 reveals an essential role for FGF signaling in the regulation of osteoblast function and bone growth. Development *130*, 3063–3074.